The role of grain boundaries in low-temperature plasticity of olivine revealed by nanoindentation

Diana Avadanii[1], Lars Hansen[2], Katharina Marquardt[3], David Wallis[4], Markus Ohl[5], and Angus Wilkinson[1]

[1]University of Oxford
[2]University of Minnesota
[3]Imperial College London
[4]University of Cambridge
[5]Utrecht University

December 7, 2022

Abstract

* Nanoindentation experiments on a high-angle grain boundary (60 * misorientation) in a pure forsterite bicrystal reveal that the interface acts as a source of dislocations. * Nanoindentation experiments on a high-angle grain boundary (60 * misorientation) in a pure forsterite bicrystal reveal that the interface acts as an obstacle to incoming dislocations, leading to pileups of dislocations. * Nanoindentation experiments on a subgrain boundary (13 * misorientation) in a pure forsterite bicrystal do not detect the impact of the interface on dislocations.

The role of grain boundaries in low-temperature plasticity of olivine revealed by nanoindentation

Diana Avadanii[1], Lars Hansen[2], Katharina Marquardt[3], David Wallis[4], Markus Ohl[5], Angus Wilkinson[6]

[1]Department of Earth Sciences, University of Oxford
[2]Department of Earth and Environmental Sciences, University of Minnesota
[3]Department of Materials, Imperial College London
[4]Department of Earth Sciences, University of Cambridge
[5]Department of Earth Sciences, Utrecht University
[6]Department of Materials, University of Oxford

Key Points:

- Nanoindentation experiments on a high-angle grain boundary (60° misorientation) in a pure forsterite bicrystal reveal that the interface acts as a source of dislocations.
- Nanoindentation experiments on a high-angle grain boundary (60° misorientation) in a pure forsterite bicrystal reveal that the interface acts as an obstacle to incoming dislocations, leading to pile-ups of dislocations.
- Nanoindentation experiments on a subgrain boundary (13° misorientation) in a pure forsterite bicrystal do not detect the impact of the interface on dislocations.

Corresponding author: Diana Avadanii, `diana.avadanii@kit.edu`

Corresponding author: Lars Hansen, `lnhansen@umn.edu`

Abstract

Rheological properties of olivine influence large-scale, long-term deformation processes on rocky planets. Studies on the deformation of olivine at low temperatures and high stresses have emphasized the importance of a grain-size effect impacting yield stress. Laboratory studies indicate that aggregates with finer grains are stronger than those with coarser grains. However, the specific interactions between intracrystalline defects and grain boundaries leading to this effect in olivine remain unresolved. In this study, to directly observe and quantify the mechanical properties of olivine grain boundaries, we conduct nanoindentation tests on well characterized bicrystals. Specifically, we perform room-temperature spherical and Berkovich nanoindentation tests on a subgrain boundary (13°, [100]/(016)) and a high-angle boundary (60°, [100]/(011)). These tests reveal that plasticity is easier to initiate if the high-angle grain boundary is within the deformation volume, while the subgrain boundary does not impact initiation of plasticity. Additionally, the high-angle grain boundary acts as a barrier to slip transmission, whereas the subgrain boundary does not interact with dislocations in a measurable manner. We suggest that the distribution of grain-boundary types in olivine-rich rocks might play a role in generating local differences during deformation.

1 Introduction

The strength of Earth's lithosphere controls a variety of geodynamic phenomena. Examples include the dip of subducting slabs (Billen & Hirth, 2007), the flexural response of oceanic lithosphere to tectonic forces (Watts & Zhong, 2000; Hunter & Watts, 2016), and the geodetically measurable surface strain rates in continental collision zones (England & Molnar, 2015). Olivine is the main constituent of Earth's upper mantle, and consequently, the deformation mechanisms operating in olivine under different geological stress and temperature conditions control the strength of the oceanic lithospheric (Watts & Zhong, 2000; Hunter & Watts, 2016; Pleus et al., 2020; Korenaga, 2020). In the portions of oceanic lithosphere supporting the most stress, the key deformation mechanism controlling long-term behaviour is low-temperature plasticity (Hansen & Kohlstedt, 2015; Mei et al., 2010). In this depth range, diffusion and recovery are relatively slow, and the rate of deformation is limited by the glide of line defects (dislocations) through the crystal lattice (Hansen & Kohlstedt, 2015; Frost & Ashby, 1982, Ch 2).

Laboratory investigations into the rheological behaviour of olivine have generated several different calibrations of flow laws for low-temperature plasticity, which present significant disagreements (e.g., Mei et al., 2010; Hansen et al., 2019; Kumamoto et al., 2017; Druiventak et al., 2011; Idrissi et al., 2016; Raterron et al., 2004). Furthermore, these flow laws disagree with geophysical measurements when extrapolated to geological conditions (e.g., Mei et al., 2010; Hunter & Watts, 2016; Watts & Zhong, 2000). Some of the disagreements among laboratory studies have been reconciled by a size effect (Kumamoto et al., 2017; Hansen et al., 2019; Koizumi et al., 2020). Kumamoto et al. (2017) predicted that samples with grain sizes typical of the upper mantle (0.1–1 cm) are weaker than the finer grained (1–10 µm) samples tested in laboratory studies. The mechanical data of Hansen et al. (2019) highlight that the yield stress of relatively pristine olivine does decrease with increasing grain size, but the steady-state flow stress is grain-size independent after strain hardening. The grain-size sensitivity of the yield stress of previously undeformed olivine aggregates demonstrates that the macroscopic yield stress is fundamentally controlled by the density of grain boundaries in the material (Hansen et al., 2019). The measurements of residual stress by Wallis et al. (2020) in the samples from Hansen et al. (2019) confirm that long-range interactions among dislocations represent the underlying cause for the observations of strain hardening, but the specific relationships among dislocations, grain boundaries, and long-range interactions remain poorly constrained (Hansen et al., 2019; Wallis et al., 2020).

The decrease in yield stress with an increase in grain size is a well documented phenomenon in engineering materials generally referred to as the Hall-Petch effect. Models of this effect rely on the mechanisms of slip transfer between grains and/or dislocation generation at grain boundaries (for a review, see Cordero et al., 2016). However, these models are difficult to test with existing data for olivine. Previous laboratory investigations of low-temperature plasticity involved experiments with either single-crystal (e.g., Demouchy et al., 2013; Gaboriaud et al., 1981; Goetze & Evans, 1979; Idrissi et al., 2016; Hansen et al., 2019) or polycrystalline samples (e.g., Druiventak et al., 2011; Hansen et al., 2019; Katayama & Karato, 2008; Mei et al., 2010; Raterron et al., 2004) at thermo-mechanical conditions attempting to approximate the upper mantle (e.g., Raterron et al., 2004; Mei et al., 2010). In these experiments it is challenging to unpick the microphysics associated with interactions between dislocations and grain boundaries. While previous nanoindentation tests (Kumamoto et al., 2017) and transmission electron microscopy investigations of deformed olivine indicate that grain boundaries might act as dislocation sources (Thieme et al., 2018; Wallis et al., 2020), we lack direct observations of this phenomenon. For example, Kumamoto et al. (2017) highlighted differences in mechanical data representative of small volumes, and documented that the initiation of plasticity requires smaller stresses in a predeformed polycrystalline sample compared to an annealed single crystal. These observations imply that either the grain boundaries or the high initial dislocation density promote dislocation generation in the polycrystalline sample compared to the single crystal (Kumamoto et al., 2017). Furthermore, while some studies have indicated that different types of grain boundaries impact slip transfer in olivine (e.g., Ferreira et al., 2021; Bollinger et al., 2019), the microphysics of the interactions between different grain boundaries and dislocations in olivine remain unresolved in both low-temperature plasticity and deformation at high temperatures .

This study aims to clarify the role of grain boundaries in low-temperature plasticity of olivine, and contributes towards explaining the grain-size effect observed by Hansen et al. (2019). In this study, we conduct nanoindentation experiments and high-resolution microscopy on high-purity forsterite (Mg_2SiO_4) bicrystals as an analog to iron-bearing olivine. Our experiments and microstructural analyses aim to quantify the role of subgrain boundaries and high-angle grain boundaries in slip transmission and dislocation generation. The only free variable in our experimental set-up is the vertical grain boundary between two crystals free of dislocations, which are symmetric across the interface.

2 Materials and Methods

2.1 Samples

We use pure forsterite bicrystal samples to investigate a subgrain boundary (SB, 13°, [100]/(016)) (e.g., Gardés et al., 2021; Adjaoud et al., 2012) and a high-angle grain boundary (HAGB, 60°, [100]/(011)) (e.g., Fig 7 of Adjaoud et al., 2012). In our samples, the [100] axis represents the shared axes of rotation between the two crystals and (016) and (011) represent the plane parallel to the boundary plane in the subgrain sample and the high-angle grain boundary sample, respectively. The bicrystals were prepared using the wafer-bonding technique (Heinemann et al., 2001, 2005; Hartmann et al., 2010). This technique generates synthetic grain boundaries free of induced deformation and chemical contamination. The grain-boundary misorientation angle is precisely controlled to generate symmetric, low-energy, and near-coincidence grain boundaries (Hartmann et al., 2010; Heinemann et al., 2001, 2005; Marquardt et al., 2015; Adjaoud et al., 2012). Samples similar to the HAGB sample used in this study have previously been characterized in detail, revealing that the grain boundary width is less than 1 nm and the plane is faceted on the nanometre-scale (see Fig 9, Marquardt & Faul, 2018). Similar subgrain boundaries to the SB sample have been described by Heinemann et al. (2005) as arrays of edge dislocations with periodic spacing and a Burgers vector of [001]. Further structural descriptions can be found in Adjaoud et al. (2012). Schematic illustrations of the sample geometries are presented in Figure 1. We use one bicrystal sample for the investigation of the subgrain boundary (SB) and three similar samples for the investigation of the high-angle grain boundary (HAGB).

2.2 Micromechanical testing

We used nanoindentation to examine the mechanical properties of our samples at high spatial resolution (e.g., Vachhani et al., 2016). We placed arrays of equally spaced indents into the bicrystals so that the indents lie at varying distances from the grain boundary (Table 1). We categorize indents into three main groups: 1) indents within one of the crystals, 2) indents near the grain boundary, such that the grain boundary intersects the residual impression of the indent, and 3) indents directly on top of the boundary such that the residual impression is centered on the boundary. Nanoindentation tests were conducted on a Nano Indenter® G200, using continuous stiffness measurement on the loading segment of the experiment (Oliver & Pharr, 1992). We employed both Berkovich and spherical indenter tips and conducted tests to a variety of maximum indentation depths. Table 1 provides details of each experiment. The experiments were performed at a target indentation strain rate (loading rate divided by the load) of 0.05 s^{-1}. Further details regarding placement of indents with respect to the grain boundary can be found in Supplementary Materials (Figures A1, A2, A3, A4).

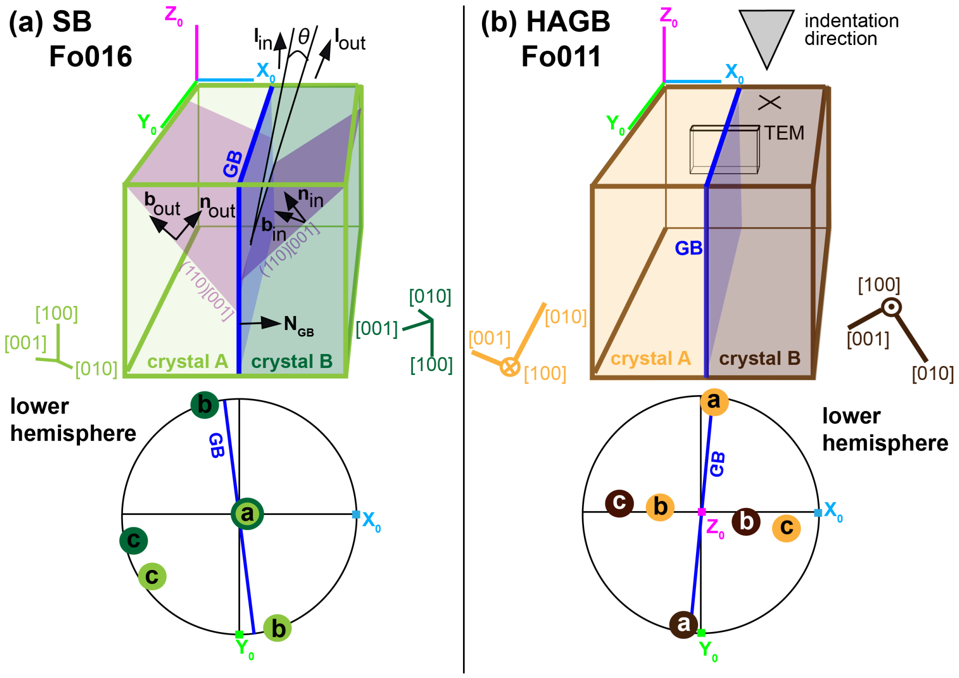

Figure 1. a) Schematic depicting the subgrain-boundary geometry and lower-hemisphere projection of the SB bicrystal. Examples are depicted of a slip system with an incoming slip direction $\mathbf{b}_{\text{in}}$ towards the subgrain boundary and an outgoing slip system with the direction vector $\mathbf{b}_{\text{out}}$. b) Schematic depicting the grain-boundary geometry and lower-hemisphere projection of the HAGB bicrystal. The indented surface is perpendicular to $\mathbf{Z}_0$. Note that the indentation direction is consistent between crystals A and B in both samples.

Table 1. Summary of experiments on bicrystal samples with a subgrain boundary (SB) or high-angle grain boundary (HAGB). Experiments were conducted using either sharp or spherical tips, the latter of which had variable nominal radii, R_{n}. The effective radius at the end of elastic loading is indicated for each tip as R_{eff}. The lower-case letter at the end of the array number in the HAGB bicrystal corresponds to different samples. The number of tests is expressed as the number of columns times the number of rows of indents across the boundary.

Tip	SB Fo016					HAGB Fo011					
	Array	Tests	Spacing (μm)	Max depth (nm)	Microscopy HREBSD	Array	Tests	Spacing (μm)	Max depth (nm)	Microscopy HREBSD	TEM
Berkovich	array1	6x4	40	1000		array4a	3x8	10	500		
	array2	1x4	40	1000		array11f	3x10	12	700	Ind11,12	Ind11
	array3	10x6	15	700	Ind25	array12f	3x10	13	700	Ind1, 2, 5, 6	
	array8	4x7	8	350	Ind6, 11, 14						
$R_{\text{eff}} \approx 7\mu\text{m}$	array1	6x6	30	600							
$R_{\text{n}} = 5\mu\text{m}$	array4	3x8	15	600	Ind11,14	array2a	3x10	15	700	Ind11, 14	
$R_{\text{eff}} \approx 6\mu\text{m}$						array3a	3x5	15	500	Ind1	
$R_{\text{n}} = 5\mu\text{m}$	array10	3x8	13	600	Ind16	array12e	3x8	13	600	Ind11, 16, 17, 20, 21	Ind11
$R_{\text{eff}} \approx 4\mu\text{m}$	array11	3x8	13	600		array13e	3x8	13	600		Ind14
						array14e	3x8	13	600		Ind4

2.3 Data Analysis

2.3.1 Spherical nanoindentation

In this study, we use three different spherical tips with nominal radii, R_n, of 5 or 10 μm. We analyze data from spherical indents using a calibration routine adapted from W. Li et al. (2013) using three reference materials with different Young's moduli (fused silica, glassy carbon, sapphire) and outlined in detail by Avadanii et al. (2022). This routine generates a calibrated function for the effective radius, R_eff, and the machine stiffness, S_mach, as a function of load for each tip (Table 1).

We transform the load and displacement into stress and strain following the method proposed by Kalidindi & Pathak (2008) and Pathak & Kalidindi (2015). We calculate the indentation stress, σ, and strain, ϵ, as

$$\sigma = \frac{P}{\pi a^2}, \tag{1}$$

$$\epsilon = \frac{4h^*}{3\pi a}, \tag{2}$$

where P is the reported load corrected for the point of zero load, a is the contact radius, and h^* is the reported displacement corrected for machine stiffness and the point of zero displacement. We calculate the contact radius as $a = \frac{S^*}{2E_\mathrm{eff}}$, where S^* is the corrected contact stiffness, and E_eff is the effective Young's modulus. We correct the reported displacement, h_rep, according to

$$h^* = h_\mathrm{rep} - \frac{P}{S_\mathrm{mach}} + \frac{P}{S_\mathrm{default}} - h_0, \tag{3}$$

where S_default is the default machine stiffness during data collection ($S_\mathrm{default} = 3.7 \times 10^7$ N/m) and S_mach is the stiffness for each indenter-tip pair determined in a manner similar to W. Li et al. (2013) and following Avadanii et al. (2022). The term h_0 represents the error in the default determination of the point of zero displacement and zero load. Adapting the formulation proposed by Kalidindi & Pathak (2008), we determine h_0 by minimizing the residual function (Breithaupt et al., 2017; Avadanii et al., 2022)

$$r = \sum \left\| \frac{3(P_\mathrm{rep} - P_0) - 2S(h_\mathrm{rep} - h_0)}{S^2} \right\|. \tag{4}$$

We calculate E_eff for each indent by using the calibrated effective radius, R_eff, and fitting the elastic loading segment with the Hertzian relationship

$$h_\mathrm{e} = P^{2/3}\left(\frac{4}{3}\sqrt{R_\mathrm{eff}}E_\mathrm{eff}\right)^{-2/3}, \tag{5}$$

$$\frac{1}{E_\mathrm{eff}} = \frac{1-\upsilon_\mathrm{s}}{E_\mathrm{s}} + \frac{1-\upsilon_\mathrm{i}}{E_\mathrm{i}}, \tag{6}$$

where E_eff is the effective Young's modulus, $\upsilon_\mathrm{s} = 0.24$ is the Poisson's ratio of the sample, $\upsilon_\mathrm{i} = 0.07$ is the Poisson's ratio of the diamond tip, E_s is the unknown Young's modulus of the sample, and $E_\mathrm{i} = 1141$ GPa is the Young's modulus of the diamond tip.

In most of our experiments, the transition between elastic and plastic deformation is marked by a burst of displacement in the load-displacement data and of strain in the stress-strain curves, often referred to as a pop-in. Using Hertzian mechanics described in Equation 6, the load at pop-in, $P_{\text{pop-in}}$, and the corresponding effective tip radius at the pop-in, $R_{\text{eff-pop-in}}$, we calculate the maximum shear stress immediately beneath the surface, assuming an elastically isotropic solid (Morris et al., 2011; Johnson, 1970),

$$\tau_{\max} = 0.31 \left(\frac{6 P_{\text{pop-in}} E_{\text{eff}}^2}{\pi^3 R_{\text{eff-pop-in}}^2} \right)^{1/3}. \tag{7}$$

We also estimate the resolved shear stress on each slip system using the Schmid factor (Schmid & Boas, 1950). However, the magnitude and orientation of the principle stresses are nonuniform under spherical indents, and therefore the Schmid factor is also spatially variable. As a practical simplification, we calculate the Schmid factor, s, assuming the maximum compressive stress is parallel to the indentation direction, which is accurate for points in the sample directly in line with the center of the indent.

2.3.2 Berkovich nanoindentation

Berkovich nanoindenter tips are three-sided pyramids that are self similar, which results in constant effective indentation strain of 8% regardless of the indentation depth (see Chapter 3 in Fischer-Cripps & Nicholson, 2004). For these tests, the effective Young's modulus is calculated as (Oliver & Pharr, 1992)

$$E_{\text{eff}} = \frac{\sqrt{\pi}}{2} \frac{S}{\sqrt{A}}, \tag{8}$$

where S is the measured contact stiffness and A is the contact area. For a Berkovich indenter, the contact area is defined by

$$A(h_c) = 24.5 h_c^2 + C_1 h_c^1 + C_2 h_c^{1/2} + ... + C_8 h_c^{1/28}, \tag{9}$$

where the contact depth, h_c, is defined as

$$h_c = 0.72 \frac{P}{S}. \tag{10}$$

The constants C_1 through C_8 are determined by calibration with an isotropic material of known elastic moduli, in our case fused silica (Oliver & Pharr, 1992). Finally, the hardness, H is given by

$$H = \frac{P}{A}. \tag{11}$$

2.4 Microstructural characterization

2.4.1 HR-EBSD

We investigated the residual impressions of the nanoindents using high-angular resolution electron backscatter diffraction (HR-EBSD). For this purpose, we collected EBSD patterns using an Oxford Instruments NordlysNano EBSD detector and stored them for subsequent cross-correlation analysis. We mapped regions including indents placed in the vicinity of the subgrain boundary or grain boundary using step sizes of 0.05–0.15 µm. We measured small distortions of diffraction patterns by cross correlating regions of interest (ROIs) within a diffraction pattern with the same ROIs in a reference diffraction pattern (Britton & Wilkinson, 2011, 2012; Wilkinson, 2006; Wilkinson et al., 2006; Wallis et al., 2016, 2019). Similar to Wallis et al. (2016), we used 100 overlapping ROIs of 256 x 256 pixels within each diffraction pattern of 1344 x 1024 pixels. We selected one reference point in each crystal, at a distance of at least 5 µm from the margin of the imprint left by the indents. Small shifts between the ROIs in the patterns are used to quantify the lattice distortion, which is comprised of the elastic strain and the lattice curvature. In-plane stress tensor components are calculated assuming linear elasticity from measured strains. These stresses are calculated relative to the stress state at the selected reference point in the undeformed crystal (for details, see Wallis et al., 2019). We assume the stresses acting normal to the specimen surface are fully relaxed. GND densities are calculated for olivine from the lattice curvature via the procedure established by Wallis et al. (2016, 2019).

2.4.2 Transmission electron microscopy

To investigate the interaction between dislocations and the HAGB beneath spherical and Berkovich indents, we imaged thin foils using transmission electron microscopy (TEM). We prepared the TEM foils perpendicular to the HAGB as depicted in Figure 1b, using FEI Helios® Nanolab G3 Dualbeam system at the Utrecht University microscopy center (e.g., Figure 3, Liu et al., 2016). We sputter-coated the samples with a 9 nm layer of Pt/Pd and then used a standardized procedure to mill and lift out the TEM foil (e.g., Ohl et al., 2020). We imaged two liftouts in the HAGB bicrystal (spherical indents 11 in array12e and 14 in array13e, Table 1) using an FEI Talos® F200X with an acquisition acceleration voltage of 200 kV and a beam current of 5–10 nA, also at the Utrecht University microscopy center (e.g., Ohl et al., 2020). We additionally imaged two liftouts from the HAGB bicrystal (Berkovich indent 11, array11f, and spherical indent 4, array14e, Table 1) using a JEOL® 2100F microscope at Imperial College London. The microscope was operated with an acquisition acceleration voltage of 200 kV, and an emission current of 120 µA.

2.5 Analysis of slip transfer

For indents in the vicinity of the boundary, we can estimate the geometric constraint on transmission of slip from one grain to another. We use average crystal orientations from the EBSD data and knowledge about the boundary geometry to calculate the geometrical relationships among different systems on each side of the boundary (for a review, see Bayerschen et al., 2016; Javaid et al., 2021), as depicted in Figure 1a. We use the formulation proposed by Luster & Morris (1995) to calculate a geometrical factor, m',

$$m' = (\mathbf{n}_{\text{in}} \cdot \mathbf{n}_{\text{out}})(\mathbf{b}_{\text{in}} \cdot \mathbf{b}_{\text{out}}), \tag{12}$$

where $\mathbf{n}_\mathrm{x}$ are unit vectors normal to the slip plane, $\mathbf{b}_\mathrm{x}$ are unit vectors along the slip direction, and the subscripts denote incoming and outgoing slip systems similar to Figure 1a. We note that, although slip systems in either crystal are denoted as incoming or outgoing, the actual direction of dislocation motion is irrelevant in these calculations. This factor ranges from 0 for the boundary acting as a complete barrier, to 1 for the boundary being transparent to dislocation motion (Javaid et al., 2021). However, this formulation only depends on the misorientation between crystals and does not depend on the orientation of the boundary plane. In our experiments, we know the trace and the inclination of the boundary in each bicrystal, which allows us to calculate a geometrical boundary transmissibility factor, M, proposed by Shen et al. (1986) to account for the boundary inclination,

$$M = (\mathbf{l}_\mathrm{in} \cdot \mathbf{l}_\mathrm{out})(\mathbf{b}_\mathrm{in} \cdot \mathbf{b}_\mathrm{out}), \tag{13}$$

$$\mathbf{l} = \mathbf{n} \times \mathbf{N}_\mathrm{B}, \tag{14}$$

where $\mathbf{l}$ is a unit vector along the intersection between the slip plane and the boundary plane, and $\mathbf{N}_\mathrm{B}$ is the normal to the boundary plane. In the samples described in Figure 1, $\mathbf{N}_\mathrm{B}$ is [016] for the SB sample and [011] for the HAGB sample. Due to the high symmetry of the boundary configuration, $\mathbf{N}_\mathrm{B}$ is the same for both crystals in each bicrystal (Hartmann et al., 2010; Marquardt & Faul, 2018; Adjaoud et al., 2012). In Equation 14, slip transfer is favoured for the combination of slip systems that minimize the angle between $\mathbf{l}_\mathrm{in}$ and $\mathbf{l}_\mathrm{out}$, and the angle between $\mathbf{b}_\mathrm{in}$ and $\mathbf{b}_\mathrm{out}$ in Figure 1 (Bayerschen et al., 2016; Javaid et al., 2021). These factors still only quantify the geometrical misalignment of the incoming and outgoing slip systems, and additional criteria (e.g., minimised residual Burgers vector in the boundary plane) would have to be satisfied to fully predict slip transmission across a grain boundary (Bayerschen et al., 2016).

3 Results

3.1 Mechanical testing

We tested the mechanical properties of the forsterite bicrystals using spherical indenters. Figure 2 presents examples of stress-strain curves derived from tests on the SB and HAGB samples with varying position relative to the grain boundary. A key feature of these curves is the prevalence of pop-ins, which are evident as departures from the elastic modulus by strains of a few percent at near-constant stress followed by decreases in stress and strain along gradients similar to the elastic modulus before the onset of further plastic flow. In the SB sample (Figure 2a), almost all stress-strain curves exhibit pop-ins. However, indents placed on top of the boundary (i.e., those for which the residual indent overlaps the trace of the subgrain boundary) display pop-ins at lower stresses compared to those that do not intersect the subgrain boundary. In the HAGB sample (Figure 2b), the indents placed on top of the grain boundary (Figure A3) exhibit no pop in or pop ins occurring at significantly lower stresses compared to indents further away from the grain boundary, for which almost all indents have pop-ins.

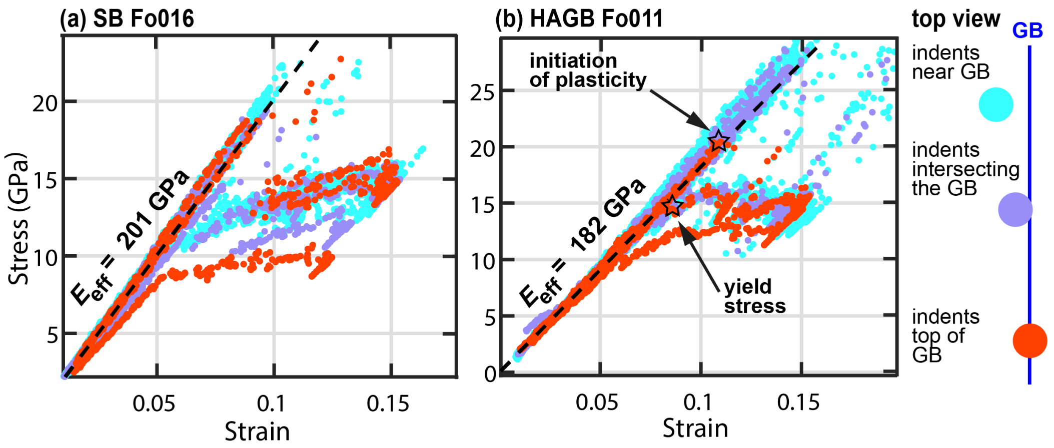

Figure 2. Selected results from spherical indentation using the 4 and 6 µm tips in Table 1 in the a) SB sample and b) HAGB sample. The diagram on the right depicts the three categories of indents: indents with a residual mark centered on the grain boundary, indents where the grain boundary intersects the residual mark but is offset from its centre, and indents in a single crystal near the grain boundary. The stars mark examples of points identified as the initiation of plasticity and therefore the yield stress. Further details of the location of indents can be found in Figures A1 and A3.

Another key feature of the stress-strain curves is the magnitude of stress reached prior to plastic deformation. Figure 2b highlights the conventions that we use in describing the initiation of plasticity and the yield stress. We refer to the initiation of plasticity as the stress at the end of the elastic-loading segment. If a pop-in is not present, then the initiation of plasticity can also be referred to as the yield stress. If a pop-in is present, the yield stress represents the projection of the plastic flow on the leastic segment (similar to Kumamoto et al. (2017)). Figure 3 displays the variations in stress at the initiation of plasticity with distance from the grain boundary in both samples. The indents lacking a pop-in are marked with red symbols. Figure 3 distinguishes among data collected with different indenter tips, due to a documented size-effect in spherical nanoindentation in which stress increases with decreasing tip radii (e.g., Pathak & Kalidindi, 2015; Kumamoto et al., 2017). Figure 3a presents data in the SB sample and highlights that the stress at the initiation of plasticity does not significantly vary with distance from the grain boundary, even for indents close to or on top of the boundary. Figure 3b presents stress at the initiation of plasticity in the HAGB sample. Unlike in the SB sample, the initiation of plasticity occurs at stresses approximately 5–15 GPa lower for indents placed on top of the grain boundary relative to typical values of those either side. These trends in the stress data in Figure 3 are consistent with the trends displayed by the load at pop-in (see Figure A6), and the corresponding shear stress (see Figure A9).

Measurements using sharp indenters test the strength of the material at an effective strain of 8%. Figure 4 displays hardness versus indentation depth for both samples. Each crystal has a corresponding colour, whereas the indents placed on top of the grain boundary are displayed in red (see Figures A2 and A4). Figure 4 exhibits a nanoinden-

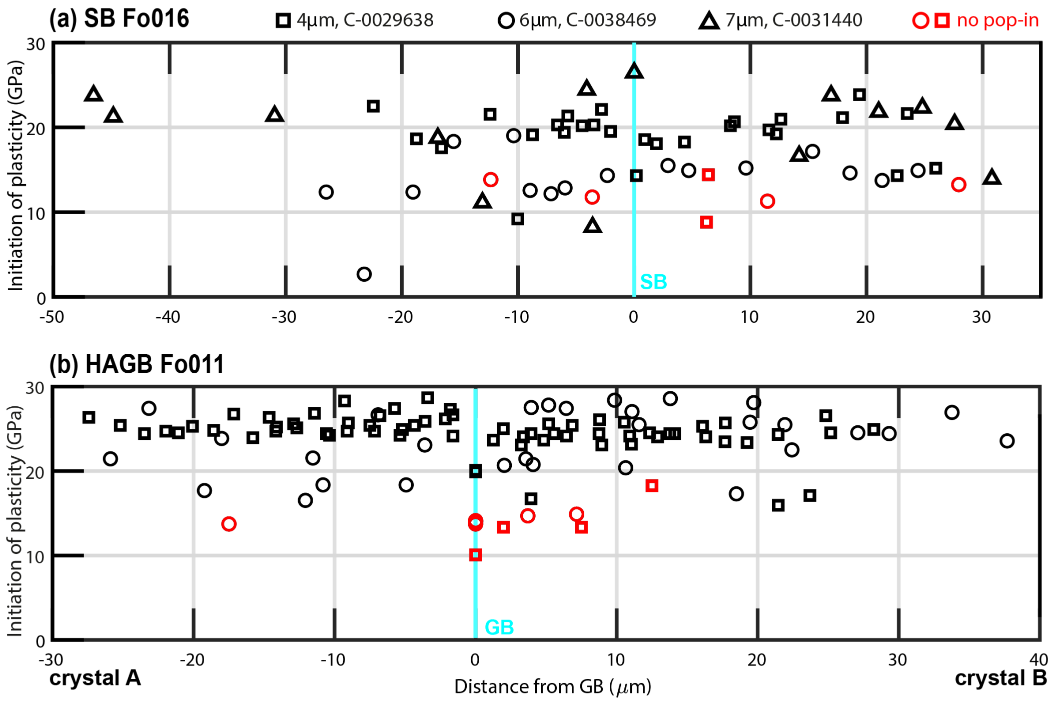

Figure 3. Summary of results from spherical indentation in the (a) SB sample and (b) HAGB sample. The black symbols correspond to the stress at the initiation of plasticity. In indents without a pop-in (red), the initiation of plasticity is equivalent to the yield stress. The variation in the load at pop-in with distance from the grain boundary, and the corresponding shear stresses are presented in Figures A6 and A9 in Supplementary Materials.

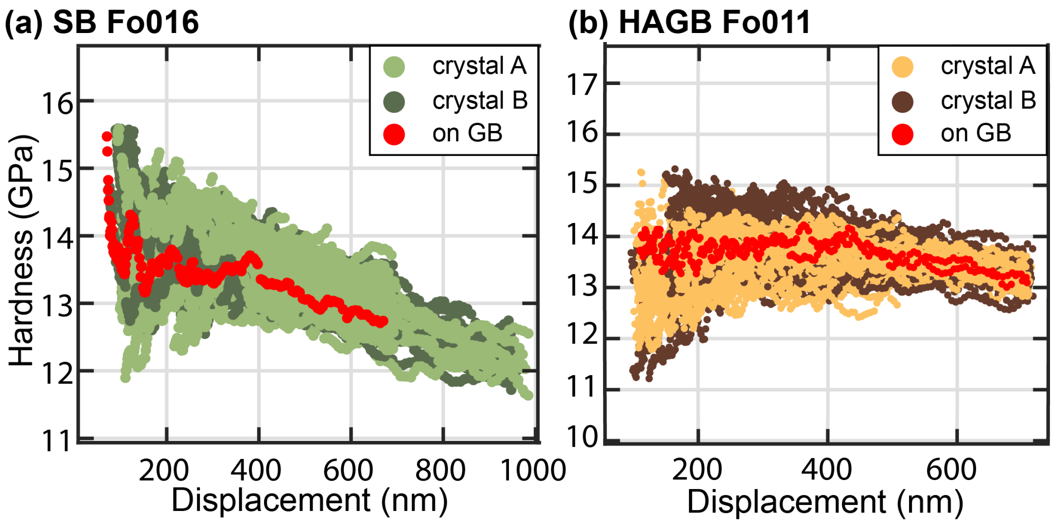

Figure 4. Summary of results using a Berkovich indenter tip (Table 1). The hardness data are coloured according to each crystal in Figure 1. The indents that left an imprint with the centre overlapping the trace of the grain boundary are marked in red (for details, see Figures A2, A4).

tation size effect, in which hardness decreases with increasing displacement. In this tertiary division of the data set with respect to the grain boundary (i.e., crystal A, or B, or on top of the interface) the indents placed on the grain boundary are similar to the indents placed in either crystal in both the SB and the HAGB samples. The load-displacement data collected using a Berkovich indenter tip does not present significant (i.e., $>$ 2–3 nm) bursts in displacement (pop-ins) (see Figure A5).

Figure 5 displays the hardness at constant depth with distance from the boundary and accounts for the variation of hardness with respect to the interface with greater detail compared to Figure 4. As illustrated in Figure 5a, the hardness measured in the SB sample is independent of distance to the boundary. The data also presents a subtle hardness contrast between the two crystals due to plastic anisotropy, with the hardnesses of crystal B being approximately 0.7 GPa lower than those of crystal A. The average hardness at 500 nm depth is 13.5 ± 0.04 GPa in crystal A and 12.8 ± 0.1 GPa in crystal B. Figure 5b demonstrates that hardnesses far from the boundary are comparable between crystals in the HAGB sample, with an average hardness at 500 nm of 13.6 ± 0.4 GPa in crystal A and 13.8 ± 0.4 GPa in crystal B. However, in contrast to the SB sample, the HAGB sample exhibits a systematic, albeit subtle, change in hardness with decreasing distance to the boundary at different indentation depths (Figure 5). In Figure 5 the indentation size effect raises the profile to higher hardnesses at shallower indentation depths. Hardness increases by a few hundred megapascals and peaks at a distance of 5 μm from the boundary, but indents placed on top of the grain boundary display hardnesses that are a few hundred megapascals lower than those far from the boundary.

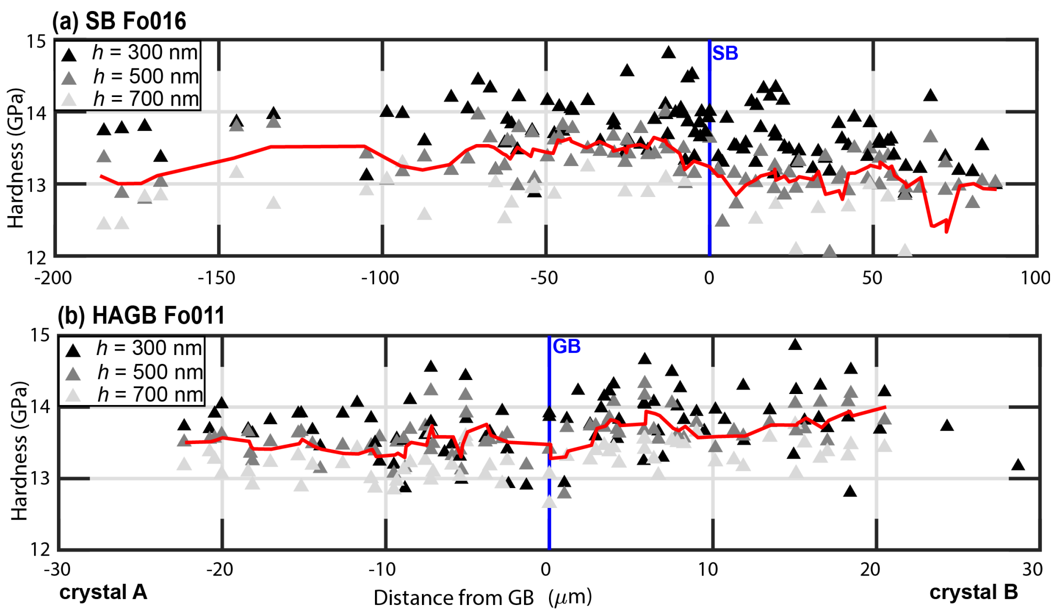

Figure 5. Summary of Berkovich nanoindentation results. The hardness at different indentations depths, h is displayed against distance from the grain boundary. The red lines represent the average hardness at 500 nm, calculated using a moving mean window spanning three data points.

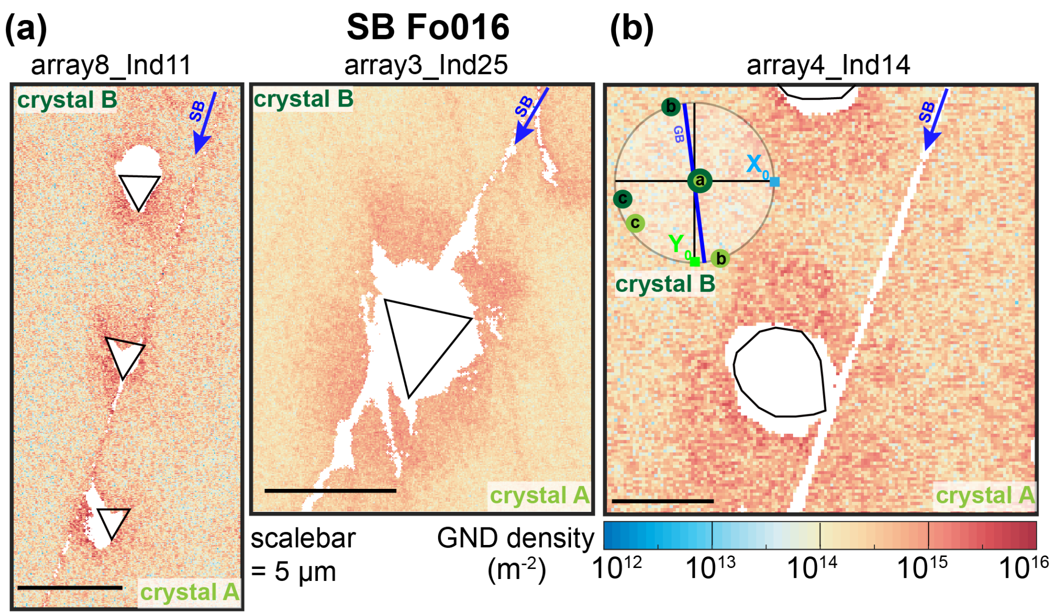

Figure 6. HR-EBSD results from the SB sample. a) Total GND densities around Berkovich indents at various distances from the subgrain boundary. b) Total GND densities around a spherical indent near the subgrain boundary. All maps have the same scalebar of 5 μm. The lower-hemisphere plot indicates the crystal orientations for each crystal. The black outline marks the indent imprint in the material. White areas mark regions that either did not index during the original EBSD mapping or failed quality criteria during the HR-EBSD cross-correlation procedure.

3.2 Microstructural characterization

Microstructural characterization with HR-EBSD reveals significant accumulations of geometrically necessary dislocations (GNDs) around indents. Figure 6 presents maps in the SB sample around sharp and spherical indents. This particular crystal orientation, with [100] perpendicular to the specimen surface, is subject to elevated levels of background noise in the GND density calculation for typical olivine slip systems (see Figure 8 in Wallis et al., 2019). The indents are surrounded by zones of elevated GND density, with values $> 10^{15}$ m^{-2}. Figure 6a displays GND densities around Berkovich indents positioned at varying distances from the subgrain boundary. The middle indent is centered in crystal B and intersects the subgrain boundary. Consequently, elevated GND densities are also present in crystal A around the same indent. However, the indent in crystal A with a center at ≈ 1.5 µm from the subgrain boundary does not exhibit detectable dislocations in crystal B. In Figure 6, the middle panel presents a Berkovich indent centered over the subgrain boundary. This indent does not exhibit GNDs with a symmetric distribution in both crystals. The corresponding hardness for this indent is lower than the indents in the bulk crystal (Figure 5b). Figure 6b presents elevated GND densities around a spherical indent with the center ≈ 2.3 µm from the subgrain boundary. This indent exhibits elevated GND densities in crystal B, but essentially no detectable GNDs in crystal A.

Figure 7 presents GND densities in the HAGB sample. The GND density is asymmetrically distributed around indents and reaches values $> 10^{15}$ m^{-2}. The grain boundary abruptly interrupts the distributions of GND density surrounding both spherical and Berkovich indents placed nearby the grain boundary. This interaction between the GND-density distribution and the grain boundary is most evident for indents within ≈ 7 µm of the boundary. Indents placed on top of the grain boundary do exhibit elevated GND densities in both crystals. The proportions of the total GND density made up of dislocations of different slip systems are presented in Figure A10.

We calculate the uniaxial Schmid factor in the single crystals for common slip systems in olivine (e.g., Tommasi et al., 2000; Mussi et al., 2014; Wallis et al., 2020) and display it in Table 2. Due to the symmetric nature of each bicrystal, the estimated Schmid factors are approximately the same in both crystals of each bicrystal. Notably, crystals in the SB sample are unfavourably oriented for all the slip systems considered ($s < 0.1$ in all cases), with [001] and [100] within 3° of the sample surface and normal to the sample surface, respectively. In contrast, crystals in the HAGB sample are well aligned ($s > 0.3$) for slip on the [001]$\{hk0\}$ and [001](010) slip systems.

We calculate several geometrical factors to assess the transparency of the boundaries to slip transfer and present them in Figure 8. The m' factor is calculated using Equation 12 and quantifies the slip transmission between an incoming and outgoing slip system across a boundary (Figure 1a), with values of 1 for a perfectly transparent boundary and 0 for a boundary acting as a perfect barrier. The values of m' for the SB sample suggest near perfect transmission for the same incoming and outgoing slip system due to the small misorientation between the two crystals (13°). Slip transfer between

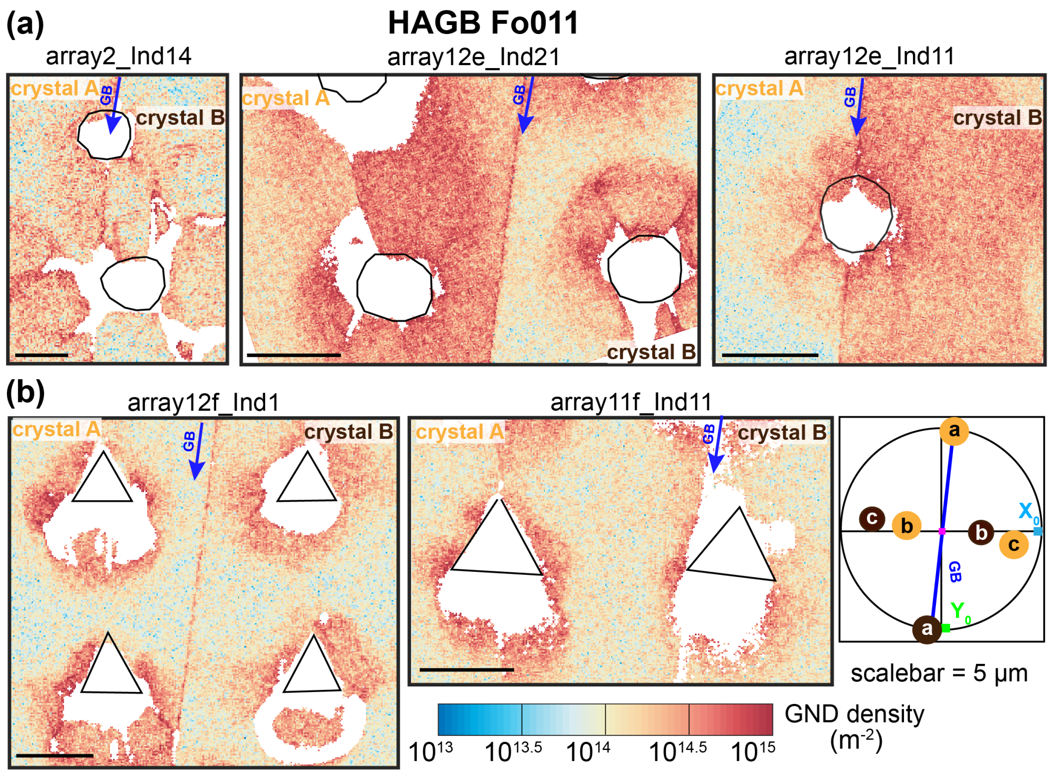

Figure 7. HR-EBSD maps around indents in the HAGB sample. a) Total GND densities around spherical indents at various distances from the grain boundary. b) Total GND densities around Berkovich indents near the grain boundary. All maps have the same scalebar of 5 μm. The lower hemisphere plot indicates the crystal orientations for each crystal. The black outline marks the indent imprint in the material. White areas mark regions that either did not index during the original EBSD mapping or failed quality criteria during the HR-EBSD cross-correlation procedure.

Table 2. Schmid factor, s, describing the relationships between the mean applied pressure and the resolved shear stresses for different slip systems considered in this study. For the HAGB sample, the indentation direction is parallel to $[0\bar{1}1]$, and for the SB sample, the indentation direction is approximately parallel to [100]. Because these bicrystals are symmetric tilt boundaries, the Schmid factor is the same for all slip systems in crystal A and B for both samples.

Slip system	SB Fo016	HAGB Fo011
[100](010)	0	0
[001](010)	0	0.43
[001](100)	0.087	0
[100](011)	0.087	0
[100](001)	0.087	0
[001](110)	0.062	0.35
[001](130)	0.029	0.43

different slip systems is also potentially easy for a significant number of the cases considered (e.g., from [001](130) to [001](010), Figure 8a). Values of m' also indicate that, by comparison, slip transfer is unfavourable in the HAGB sample for most slip systems considered (Figure 8b). The only systems favourably oriented for slip transfer are [100](001) to [100](011) and [100](011) to [100](010). The M factor is also a geometrical factor quantifying slip transmission, but additionally accounts for the tilt of the boundary according to Equation 14. In our samples, the boundary is subvertical, with a tilt of $\approx 2°$, which we approximate as vertical in this analysis. In both samples, the values of the M factor predict that the boundary is transparent for an increased number of slip systems compared to values of m' (Figure 8c and d).

Further detailed characterization using scanning TEM (STEM) presents evidence for the activity of different slip systems, and reveals dislocation structures present and their interaction with the grain boundary in the HAGB sample. Figure 9 characterizes spherical indent 11 (see location in Figure 7a), which is approximately centered on the grain boundary. The lower hemisphere diagram in Figure 9 corresponds to the viewing plane. Complex dislocation structures are present in both crystals. Dislocation loops are present in both crystals, which we interpret as dislocations on the [001](100) slip system. Both crystals present pile-ups of dislocations with increasing spacing further away from the grain boundary, which we interpret as dislocation activity on the [100](010) slip system. Dislocations appearing as lines are present in both crystals and suggest the activity of [001](010) slip system. Some of the dislocation structures present in both crystals, along lines perpendicular to the loading direction, could correspond to slip system activity within the [100]$\{0kl\}$ family. In addition, panel 1 in Figure 9 reveals that slip bands intersect and displace the grain-boundary plane, creating roughness with wavelengths and amplitudes of tens of nanometres. Sets of dislocations on different slip systems commonly intersect one another and, in some instances, loop segments of one dislocation type (e.g., on (100)) are pinned against dislocations of a different type (e.g., on (010)). Occasional microcracks have traces approximately parallel to those of the dislocation sets and the grain boundary, but are mostly at low angles to the specimen surface, consistent with the expectation that they form during unloading (e.g., Fang et al., 2021).

Figure 10 presents STEM characterization of a spherical indent in crystal A in the proximity of the grain boundary. The imprint of the spherical indent ends at the grain boundary and exhibits an asymmetric cross-section. The majority of the dislocation structures are present in crystal A including dislocation loops, pile-ups, and intersections of different slip systems (panel 1). The zone of high dislocation density present in crystal A terminates abruptly at the grain boundary (panel 2) with only scarce dislocations present in crystal B (panels 2 and 3). The dislocations in crystal B are loops on the (100) plane and the [001](010) slip system (e.g., panel 2). Unloading cracks are present parallel to slip bands and along the grain-boundary plane.

Figure 11 presents the dislocation structures in crystal B in the HAGB sample under a spherical indent that was stopped shortly after the initiation of plasticity. These microstructures reflect the dislocations generated during a pop-in after a longer segment of elastic loading compared to indents on the grain boundary or within its immediate

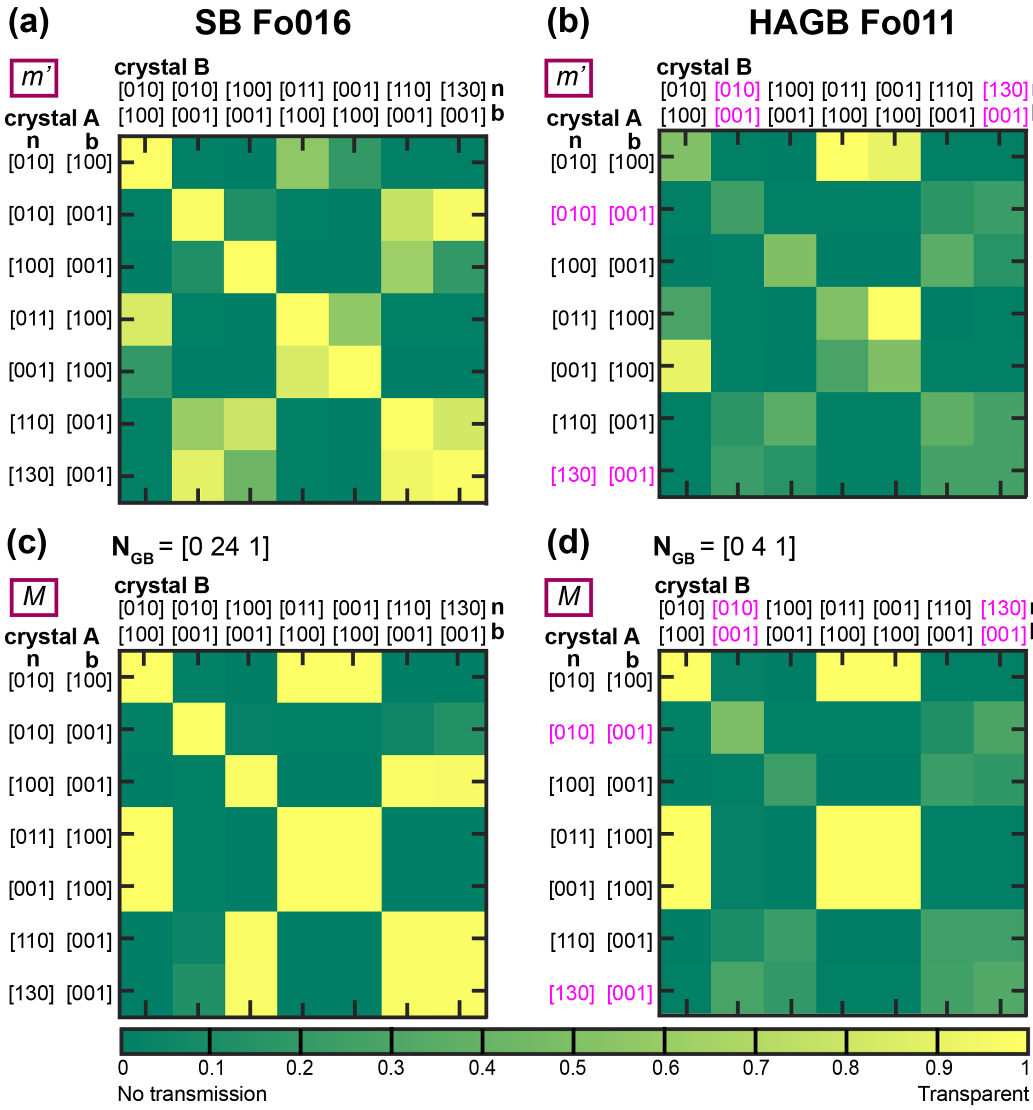

Figure 8. Geometrical transfer factor between the possible slip systems active in the bicrystals in this study. The first row represent the m' factor in a) the SB bicrystal and b) the HAGB bicrystal, and the second row displays the M factor in the a) SB bicrystal and the HAGB bicrystal. The slip systems considered are represented by the slip direction, $\mathbf{b}$, and the normal to the slip plane, $\mathbf{n}$. The normal to the grain boundary is denoted by $\mathbf{N}_{\mathrm{GB}}$. In the b) and d) panels the second and last columns and rows (with magenta labels) correspond to the slip systems with the greatest Schmid factor in Table 2.

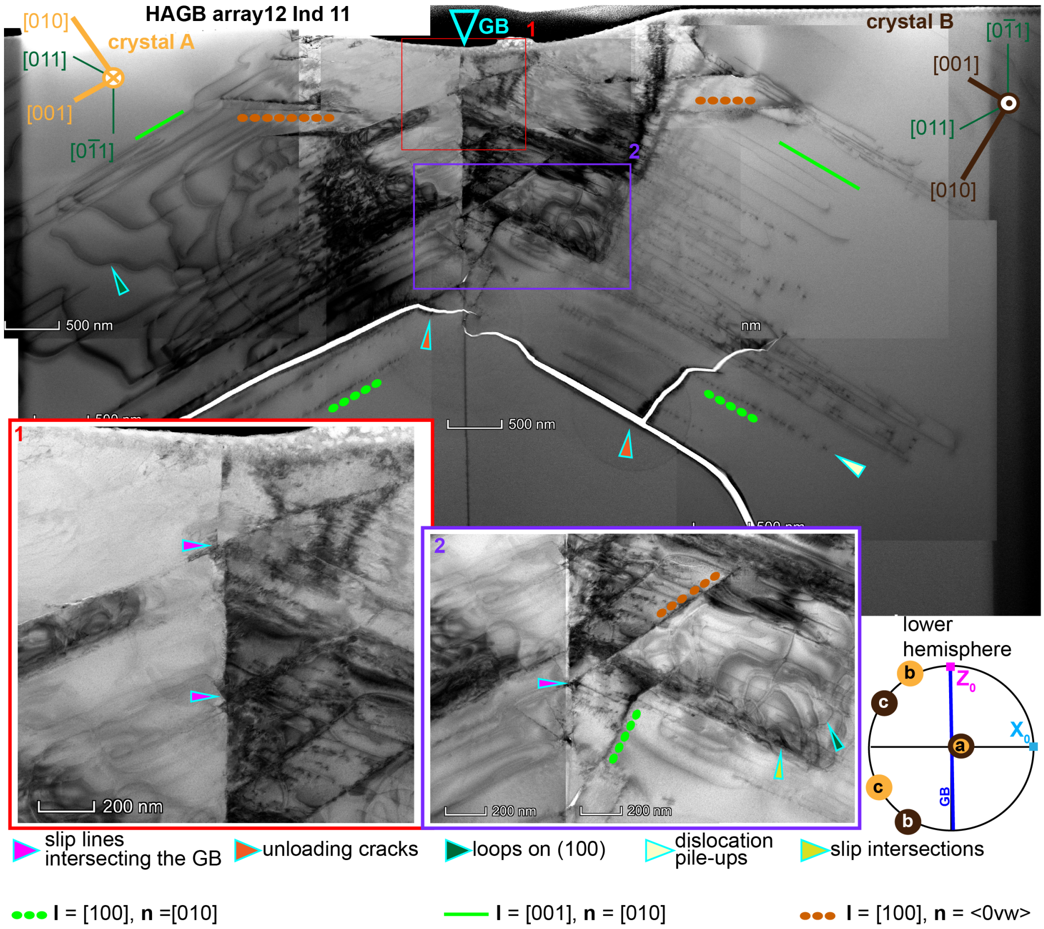

Figure 9. Bright-field STEM image of the spherical indent in Figure 7a placed on top of the high-angle grain boundary. The lower-hemisphere projection corresponds to the viewing plane. The boxes mark the position of the images at higher magnification. The corresponding stress-strain curve is presented in Figure A8a. The annotations present interpretations of possible line directions, **l**, and the slip-plane normal, **n**.

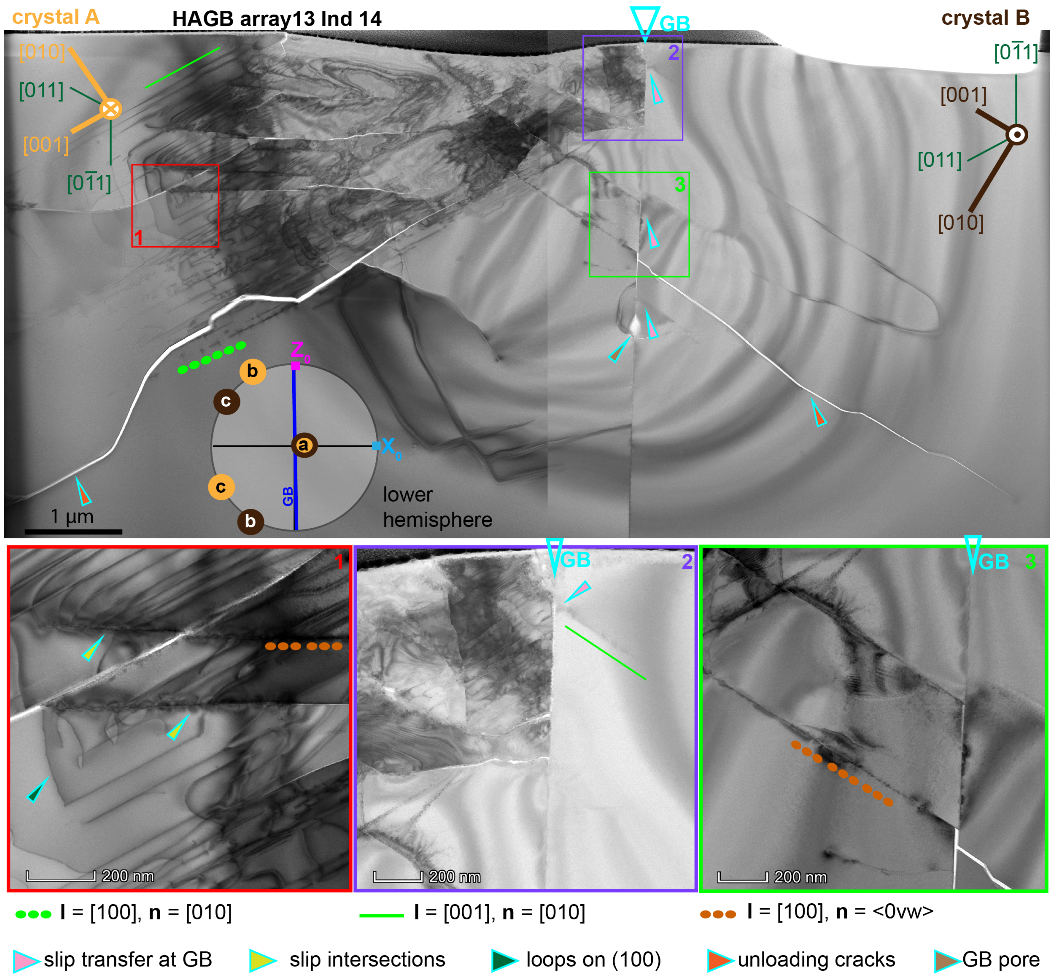

Figure 10. Bright-field STEM image of a spherical indent placed near the grain boundary in crystal A in the HAGB sample. The annotations are similar to Figure 9. The corresponding stress-strain curve is presented in Figure A8b.

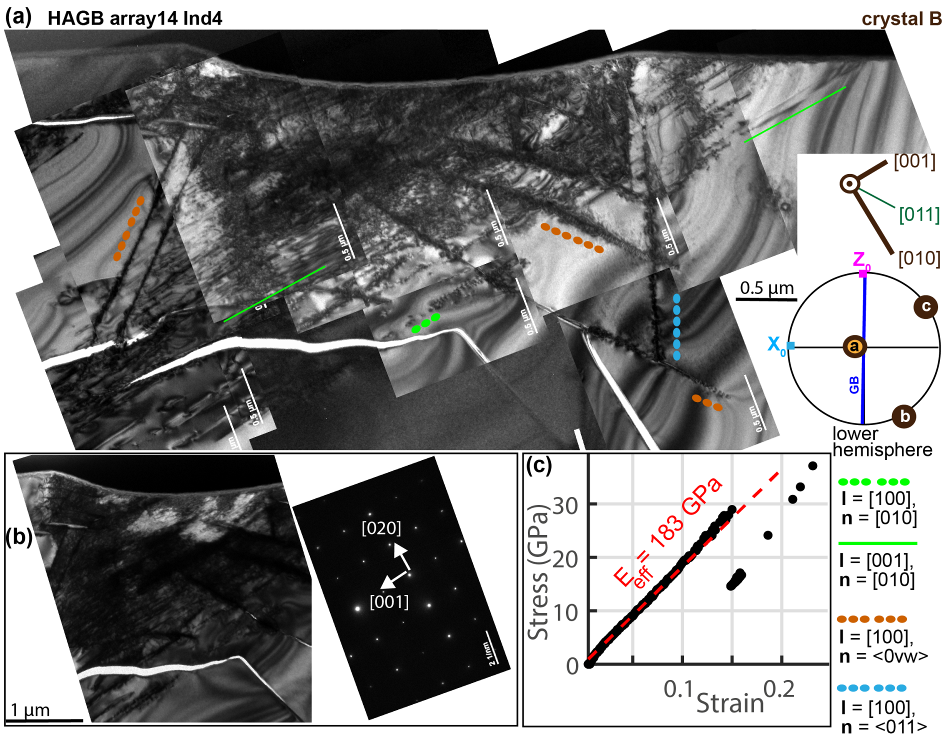

Figure 11. Bright-field STEM image of a spherical indent in the single crystal B within the HAGB sample. The corresponding stress-strain curve is presented in panel c, and highlights that there is no further flow after the pop-in event. Note that the viewing direction is flipped compared to Figures 9 and 10.

vicinity. The dislocation structures are complex, with the intersection of dislocations active on the [001](010), [100](010) (green), and different [100]$\{0kl\}$ slip systems (orange and blue). Figure 11b presents a dark-field image collected with optimal conditions for [001] and [020].

Figure 12 displays the microstructures beneath an indent made with a sharp Berkovich tip and placed in crystal B in the vicinity of the grain boundary. The dislocation structures present activity and intersections of the [100]$\{0kl\}$ (orange and blue) and [100](010) (green) slip systems. Figure 12b presents dislocations consistent with the activity of [100](001) (pink) generated under the indent and piling up at the grain boundary. An array of dislocations consistent with the activity of the [100](010) or [001](010) slip systems (green) appears on the other side of the interface. This interaction indicates slip transfer at the grain boundary from crystal B to crystal A in Figure 12b.

4 Discussion

4.1 Overview

The interaction between grain boundaries and lattice dislocations underpins a series of key phenomena in the deformation of crystalline materials, including strain hard-

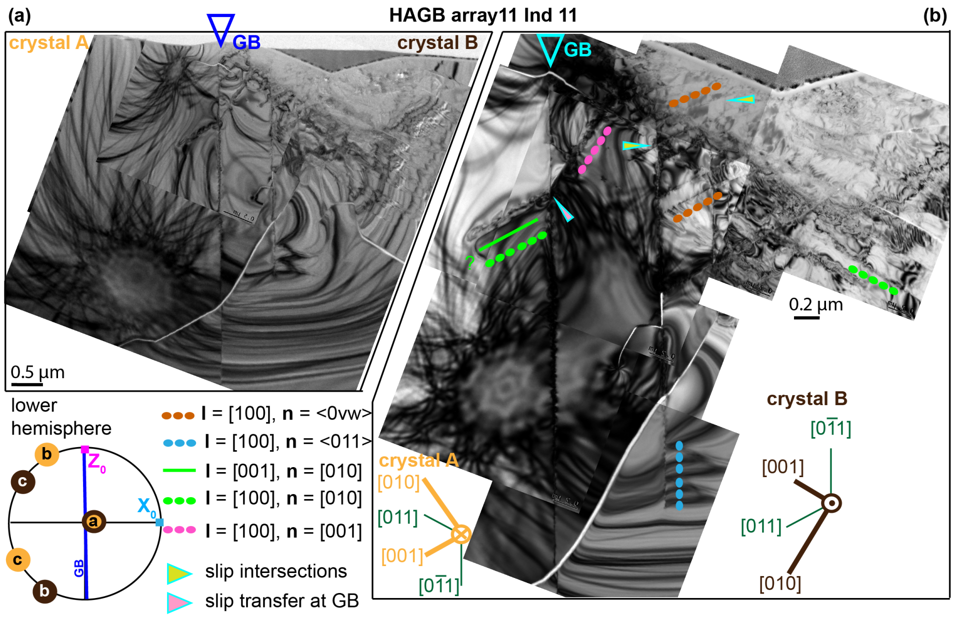

Figure 12. Bright-field STEM imaging of a Berkovich indent placed near the high-angle grain boundary in crystal B. The corresponding load-displacement curve is presented in Figure A5.

ening and the influence of grain size on yield stress (Hirth, 1972; Han et al., 2018). Experiment, theory, and numerical simulation all indicate that there are three main types of interactions: i) emission of lattice dislocations from the GB, ii) absorption of lattice dislocations at the grain boundary, and iii) slip transmission across GBs (Hirth, 1972; Javaid et al., 2021; Bayerschen et al., 2016; A.P.Sutton & R.W.Balluffi, 1995, Ch 12).

In this study, we describe nanoindentation with sharp and spherical indenters on two forsterite bicrystals with high-symmetry and low-energy boundary configurations (Figure 1) to isolate these different types of interactions. The indents were placed at varying distances from the vertical boundary (see Figures A1, A2, A3, A4). The symmetry of the crystals on each side of the boundary results in nanoindentation loading along a consistent crystal direction across the bicrystals. For the SB sample, the indentation direction is parallel to [100], whereas for the HAGB sample the indentation direction is parallel to [0$\bar{1}$1]. Although the stress field in indentation is spatially heterogeneous and impacted by crystal anisotropy, the consistent indentation direction means that distance to the boundary is the only free variable in our experiments. Our key interpretation is that the HAGB used in this study facilitates dislocation nucleation (Figures 3, 5), while also acting as a barrier to slip transmission (Figures 7, 9, 10). In contrast, the SB exhibits little impact on the initiation of plasticity or slip transmission.

Several recent investigations have focused on the impact of grain size on deformation of olivine in the low-temperature plasticity regime (Kumamoto et al., 2017; Hansen et al., 2019; Koizumi et al., 2020). When materials deform by dislocation glide during low-temperature plasticity, yield stress typically exhibits a negative correlation with grain size, traditionally described by the empirical Hall-Petch effect in metals (Hall, 1951; Petch, 1953), and documented by Hansen et al. (2019); Koizumi et al. (2020), and Kumamoto et al. (2017) in olivine. Although a wide variety of microphysical models predict this relationship (for a review, see Cordero et al., 2016), Hansen et al. (2019) identify several subsets of models that are consistent with their observations. The key processes underpinning these models rely on local defect generation prior to macroscopic yielding (i.e., microplasticity, Maaß & Derlet, 2018) and include 1) dislocation pile-up at grain boundaries that harden the material until the boundaries act as dislocation sources (Hall, 1951; Petch, 1953; Cottrell & Bilby, 1949), 2) the difficulty of emission of dislocations from grain boundaries during plastic deformation (Bata & Pereloma, 2004), 3) emission of dislocations from grain boundary ledges that subsequently lead to strain hardening (J. Li, 1963; Y. Li et al., 2016), and 4) the emission of dislocations from grain boundaries due to elastic incompatibilities that subsequently lead to strain hardening (Meyersm & Ashworth, 1982). In the following sections, we discuss observations from our experiments that help evaluate the role of these processes in the deformation of olivine.

4.2 The role of grain boundaries as a source of dislocations

Several of the models underpinning grain-size effects rely on grain boundaries acting as dislocation sources. As illustrated in Figures 3 and 5, mechanical data from our experiments display decreased hardnesses at the HAGB compared to the crystal interior, while there is no detectable change at the SB. Specifically, the reduction in the hardness at the initiation of plasticity in spherical indents provides direct evidence that the HAGB assists the generation of dislocations. This trend is consistent for deformation at strains $<$15% across the two nanoindentation techniques. In the case of the HAGB sample the stress required for generating and gliding dislocations drops from ~ 25 GPa in the crystal interior to $<$ 20 GPa in the grain-boundary region (Figure 3b). Similarly, the maximum shear stresses reached for the initiation of plasticity on the grain boundary ($<$ 10 GPa) are smaller when compared to the shear stresses required in the single crystal ($>$ 10 GPa). The shear stresses at pop-in (12.7 GPa in the HAGB sample and 15.8 GPa in the SB sample) in the single crystal approach the theoretical limit, suggesting that stress at the initiation of plasticity is controlled by the distribution of dislocation sources in the deforming volume (Figure A9) (e.g., Fang et al., 2021). In metals, similar observations using spherical nanoindentation on twin boundaries have been attributed to generation of dislocations at the twin boundary (J. Li et al., 2021). In addition, our experiments reveal that a low-energy SB, comprised of arrays of periodic dislocations with the [001] Burgers vector (Heinemann et al., 2005) is not a potent source of dislocations (Figure 3a and A9).

Detailed investigations of spherical indents placed on top of the HAGB reveal complex dislocation structures. In Figure 9, slip bands extend from the grain boundary into the crystal interior, suggesting their origin at the boundary. These dislocations could be generated from a source in the grain-boundary plane or within its immediate vicinity (A.P.Sutton & R.W.Balluffi, 1995, Ch 12). Drawing inspiration from investigations of metals, we suggest a number of hypotheses for the specific mechanism of dislocation nucleation. J. Li (1963) and Murr (1975) proposed a model of dislocation emission from grain boundaries involving grain-boundary ledges (grain-boundary dislocations accommodating grain boundary curvature) that can either act as stress concentrators mediating the nucleation of dislocation loops in the immediate vicinity of the grain-boundary plane (Varin et al., 1987; Hirth, 1972), or can be sheared in the boundary plane and generate partial slip in the crystal lattice (J. Li, 1963; Price & Hirth, 1972; Hirth, 1972). Alternatively, stress concentration in the crystal lattice could be generated by line defects in the grain-boundary plane (extrinsic grain-boundary dislocations) (Varin et al., 1987; Murr, 1981; Gleiter, 1977; Sangal et al., 1991) or by the elastic anisotropy introduced by the juxtaposed crystals (Hirth, 1972; Hook & Hirth, 1967). These models rely on the grain-boundary structure. Similar samples to the HAGB imaged in Figure 9 have been investigated using high-resolution TEM by Marquardt & Faul (2018, Fig 9) and simulated via molecular dynamics by Adjaoud et al. (2012, Fig 7). Marquardt & Faul (2018) present evidence of inclined facets as part of the grain-boundary structure, while Adjaoud et al. (2012) suggest that a lower-symmetry structure is more energetically favourable than a higher-symmetry one. Given the importance of grain-boundary structure in nucleation of dislocations, we suggest that in our experiments the high-angle boundary promotes stress concentrations and activation of dislocation sources in the crystal lattice.

4.3 Slip transmission across GBs

The difficulty of slip transmission at grain boundaries can significantly contribute to hardening and size effects (Hirth, 1972). The interactions of grain boundaries and dislocations have been studied at length in metals (for review, see Kacher et al., 2014), and in ceramics (e.g., Mitchell, 1979), resulting in a series of proposed criteria for predicting the response of the grain boundary to slip transmission (Lee et al., 1989, 1990; Bayerschen et al., 2016) (Figure 1a). These criteria include: 1) minimal slip misalignment across the boundary, which translates into M and m' factors of 1 for a perfectly aligned system (Luster & Morris, 1995; Shen et al., 1986), 2) maximised resolved shear stresses on the outgoing slip plane, and 3) minimal magnitude of the residual Burgers vector in the grain-boundary plane after transmission (Kacher et al., 2014; Bayerschen et al., 2016).

Nanoindentation tests positioned in the vicinity of the grain boundary directly test the ability of the boundary to transmit or resist dislocation motion. Previous work in metals has investigated dislocation transmission through grain boundaries by collecting load-displacement data using both spherical (e.g., Kalidindi & Vachhani, 2014; Vachhani et al., 2016) and sharp (e.g., Britton et al., 2009; Wang & Ngan, 2004; Ohmura & Tsuzaki, 2007; Voyiadjis & Zhang, 2015; Aifantis et al., 2006) indenter tips. As an illustrative example, spherical nanoindentation in Al reveals that the yield stress can increase with increasing proximity to a grain boundary (e.g., Vachhani et al., 2016). Similar effects have been observed in an Al bicrystal tested with Berkovich indentation (Aifantis et al., 2006). For our samples, spherical indentation does not reveal an increase in stress at the initiation of plasticity near either grain boundary (Figure 3b). However, as discussed above, the initiation of plasticity in most of our spherical indents is defined by a pop-in and therefore primarily relates to the processes of dislocation nucleation, rather than the ease of dislocation motion. In contrast, hardnesses measured with Berkovich indentation relate primarily to the ease of dislocation motion. We note that the hardness in the HAGB sample increases with increasing proximity to the grain boundary, and exhibits maximum values at a distance of approximately 5 µm (Figure 5b). In addition, Figure 5b also indicates that the dependence of hardness on position may be slightly different in crystal A than in crystal B. Although we assume that the tilt boundaries are perfectly parallel to the indentation direction, the plane of the HAGB is actually 2–3° from normal to the sample surface. It is possible that this small deviation underpins the differences in the hardness trends in proximity to the grain boundary. Another possible explanation is the relative orientation of the indenter tip with respect to the grain boundary in each crystal (see Figure A4), with the side of the pyramid parallel or subparallel to the grain-boundary trace in crystal B and the corner or the pyramid perpendicular to the grain-boundary trace in crystal A. This azimuthal rotation of the Berkovich tip influences the magnitude of the resolved shear stresses on each available slip system and the grain boundary beneath the indent (e.g., Chen et al., 2018; Aifantis et al., 2006; Javaid et al., 2021).

These observations of mechanical properties are supported by the theoretical predictions of slip transmission, given by m' and the M factors, and by microstructural observations of dislocation structures under the indents. When accounting for the loading direction in our experiments, the Schmid factor indicates that a limited number of slip systems are oriented such that the resolved shear stresses will promote dislocation glide in the single crystal beneath the indent, followed by pile-up at the grain boundary (Table 2). In the mechanical data, there is no observable hardening with proximity to the boundary in the SB sample at either the initiation of plasticity (Figure 3a) or at 8% strain (Figure 5a), suggesting that the subgrain boundary exerts little to no resistance to slip transfer, in line with the geometrical predictions. The hardening in the proximity of the boundary in the HAGB sample (Figure 5b) and the asymmetrical residual mark of the indent (Figure 10) both indicate that the grain boundary acts as a barrier to incoming dislocations generated beneath the indenter, as expected from the geometrical predictions in Figure 8b and d. In Figure 10, the incoming slip generated in crystal A likely represents activity of [001](010) with a uniaxial Schmid factor of 0.43 (Table 2). Crystal A also presents evidence for activity of [100]$\{0kl\}$ and [100](010), and although the uniaxial Schmid factor is 0, the non-uniform stresses under the spherical indenter (e.g., T. Li et al., 2011) could promote these slip systems. Evidence of outgoing slip systems in crystal B is present in the activity of [001](010), and the loop in the [001]$\{hk0\}$ family. According to the geometrical factors m' (Figure 8b) and M (Figure 8d), slip transfer from [001](010) to [001](010) has values of ~ 0.4 and ~ 0.6, respectively. Slip transfer from [001](010) to [001]$\{hk0\}$ has predicted values of 0.3–0.4 for M. Figure 12 presents STEM imaging of a Berkovich indent in crystal B in the HAGB sample. The figure presents evidence of slip transfer from crystal B to crystal A, albeit with slip systems that are more difficult to interpret. One interpretation could be that of slip was transferred from [100](001) to [001](010), with corresponding m' and M values < 0.1. Another interpretation could be that slip was transferred from [100](001) to [100](010), with corresponding $m' = 0.8$ and $M > 0.9$. Accounting for the significant difference in the geometrical factors within the aforementioned systems, we interpret that Figure 12 most likely displays slip transmission from [100](001) to [100](010). The slip transmission documented in Figure 12b is not associated with a pop-in, unlike in studies using Berkovich indentation nearby grain boundaries in metals (e.g., Aifantis et al., 2006; Wang & Ngan, 2004; Britton et al., 2009). Figures 10 and 12 present the grain boundary as largely intact and vertical after slip-transfer, with one example of a vertical crack along the grain boundary at the end of a dislocation pile-up (panel 3, Figure 10). In summary, our microstructural observations are in general agreement with predictions based on the geometry of the bicrystal and availabile slip systems for deformation.

4.4 Impact of grain boundaries on large-scale plasticity of olivine aggregates

In this study, we present experiments conducted on synthetic bicrystals and document the connections among mechanical properties, grain-boundary character, nucleation of dislocations, and slip transfer across grain boundaries. These observations from forsterite bicrystals shed light on the microphysics of grain-size dependent yielding in olivine aggregates. We suggest that a given type of grain boundary can contribute towards multiple mechanisms of increasing the yield stress with decreasing grain size, as exemplified by the microstructures presented in the HAGB sample in Figures 9 and 10. During macroscale deformation, grain boundaries can act as barriers to lattice dislocations either due to 1) the pre-existing dislocations in the vicinity of the grain boundary generated by local yield or 2) the grain-boundary character being unfavourable to slip transmission (Sangid et al., 2011; Hirth, 1972). Figure 9 demonstrates that grain boundaries can act as sources of dislocations and generate complex dislocation structures in their immediate vicinity (see also Wallis et al., 2020), leading to an area that is harder to penetrate by incoming lattice dislocations. These phenomena have been isolated in small-scale experiments in metals (e.g., Dehm et al., 2018; Maaß & Derlet, 2018) and underpin the temperature-dependent grain-size effect of the yield stress in bulk deformation of olivine documented by Hansen et al. (2019). Therefore, our observations support a model of hardening due to local generation of dislocations at the grain boundaries before macroscopic yielding in the experiments of Hansen et al. (2019) (i.e., microplasticity, Maaß & Derlet (2018), A.P.Sutton & R.W.Balluffi (1995, Ch 12)). Consequently, intracrystalline dislocations interacting with grain-boundary regions with an enhanced density of dislocations due to microplasticity could increase the intracrystalline stresses in fine-grained aggregates (e.g., Guo et al., 2020, 2014; Andani et al., 2020). TEM observations of single crystals of olivine deformed in the low-temperature regime and the data in Figure 11 reveal tangled dislocations and intersecting slip planes (e.g., Phakey et al., 1972; Gaboriaud et al., 1981; Druiventak et al., 2011; Wallis et al., 2020; Mussi, Cordier, & Demouchy, 2015; Mussi, Nafi, et al., 2015).

In olivine deformation, the magnitude of macroscopic strain hardening by intracrystalline back stresses is independent of grain-size of the sample, as demonstrated by Hansen et al. (2019). This observation suggests that interactions amongst dislocations generated in the crystal interior control the post-yield hardening, and there is no detectable post-yield interaction with the grain boundaries in the experiments of Hansen et al. (2019). However, according to our experiments, unfavourable grain boundaries for slip transmission lead to dislocation pile-ups of defects generated within 5 μm of a grain boundary (Figures 3 and 10). Coupling this observation with the data presented by Hansen et al. (2019), we suggest that in a polycrystalline sample, the small-scale interactions between dislocations and grain boundaries with different structure balance each other out in terms of slip transmission, resulting in strain hardening that is effectively grain-size independent.

In the context of low-temperature plasticity of olivine-rich materials under geological conditions (e.g., lithosphere bending) the distribution of grain boundaries with different abilities to transmit slip could impact local strain hardening and localization, before bulk hardening of the material (e.g., Marquardt et al., 2015; Sangid et al., 2011; Andani et al., 2020). In our experiments, the SB is transparent to slip transfer, and does not generate plasticity at stresses lower than in the bulk crystal. However, we provide evidence that during macroscale deformation, a HAGB can act as a site of microplasticity. The resulting strengthening effect of grain boundaries is particularly emphasized at small strains (A.P.Sutton & R.W.Balluffi, 1995). These differences amongst subgrain and grain boundaries documented in our experiments suggest that grain size, rather than subgrain size, is the key length scale when modelling low-temperature plasticity of olivine. Thus, our results could inform future numerical models of microstructural evolution of polycrystalline olivine (e.g., Gardner et al., 2017; Piazolo et al., 2019) and of how the relative abundance and distribution of grain boundaries influences slip transmission, and subsequent strain accommodation in the deforming lithosphere.

5 Conclusions

Nanoindentation and microstructural investigations on pure forsterite synthetic bicrystals with a subgrain boundary (13°, [100]/(016)) and a high-angle grain boundary (60°, [100]/(011)) reveal that the HAGB acts as a source for dislocations and can prevent slip transmission leading to pile-up of dislocations. In contrast, the SB does not have a detectable impact on these processes. The initiation of plasticity at high-angle grain boundaries requires lower stresses compared to the crystal interior, suggesting that some grain boundaries might act as sites of microplasticity just prior to macroscopic yield. Our results also provide evidence of interactions between dislocations and grain boundaries and support an increase in macroscopic yield stress with decreasing grain size underpinned by grain-boundary regions acting as dislocation sources. We suggest that the distribution and character of grain boundaries in olivine-rich rocks could generate heterogeneity in deformation across the lithosphere.

6 Acknowledgments

DA is grateful to the UK National Environmental Research Council, and the Oxford Doctoral Training Partnership for DPhil studentship and funding [grant number NE/L002612/1]. LH, KM, and AW acknowledge funding from UK National Environmental Research Council, via the NERC Standard Grant [grant number NE/S00162X/1]. LH acknowledges funding from the National Science Foundation [grant number NSF-EAR Grant 2022433]. DW acknowledges the support of a UKRI Future Leaders Fellowship [grant number NE/M000966/1], and the Netherlands Organisation for Scientific Research, User Support Programme Space Research [grant number ALWGO.2018.038].

Appendix A Appendix Section

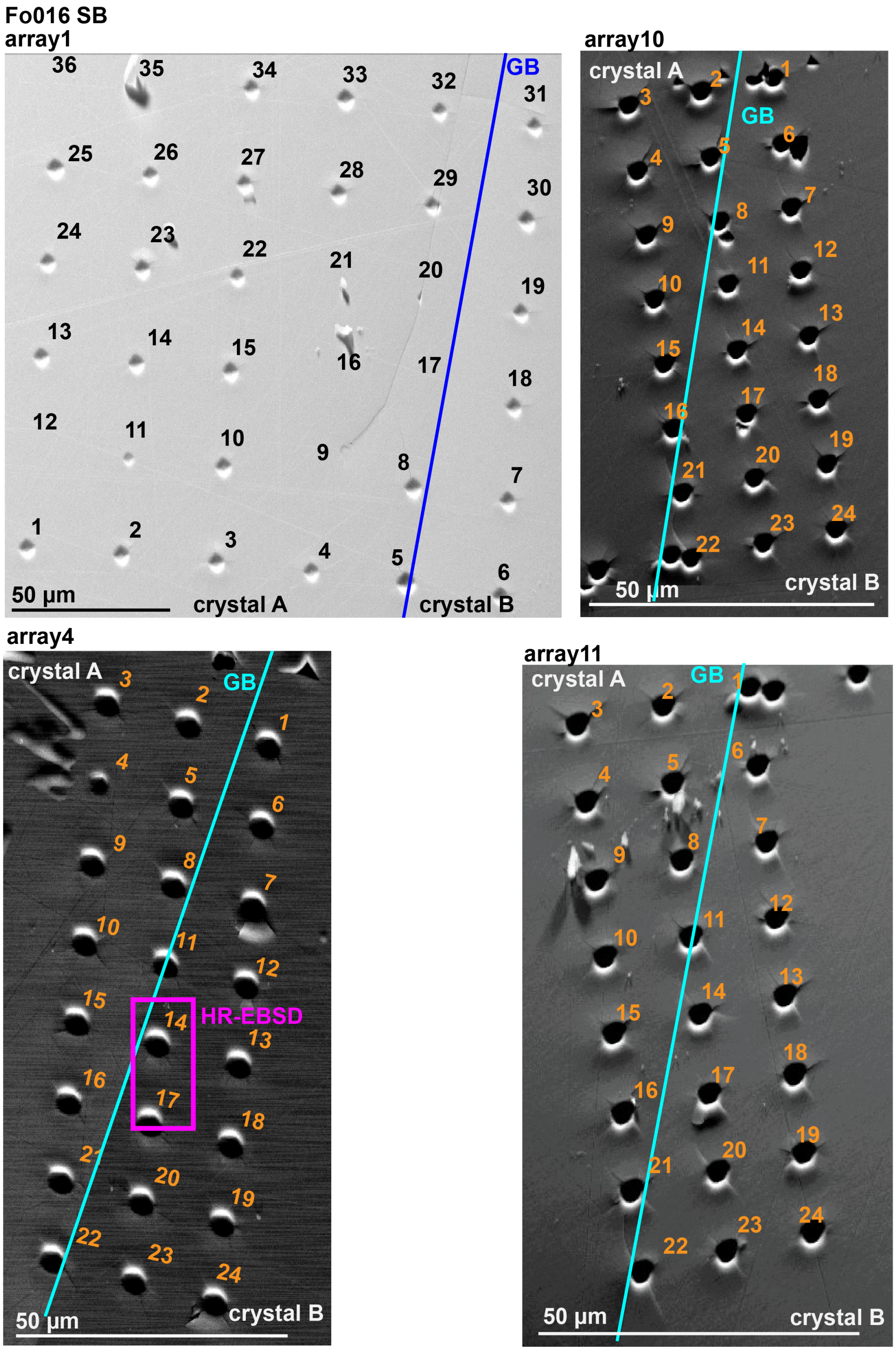

Figure A1. Backscatter images depicting the arrays placed in the SB sample with a spherical indenter as detailed in Table 1. The position of the further microstructural investigations with respect to the other indents and the grain boundary is marked by the magenta square. The numbers hear each indent correspond to the order in which the indents were placed.

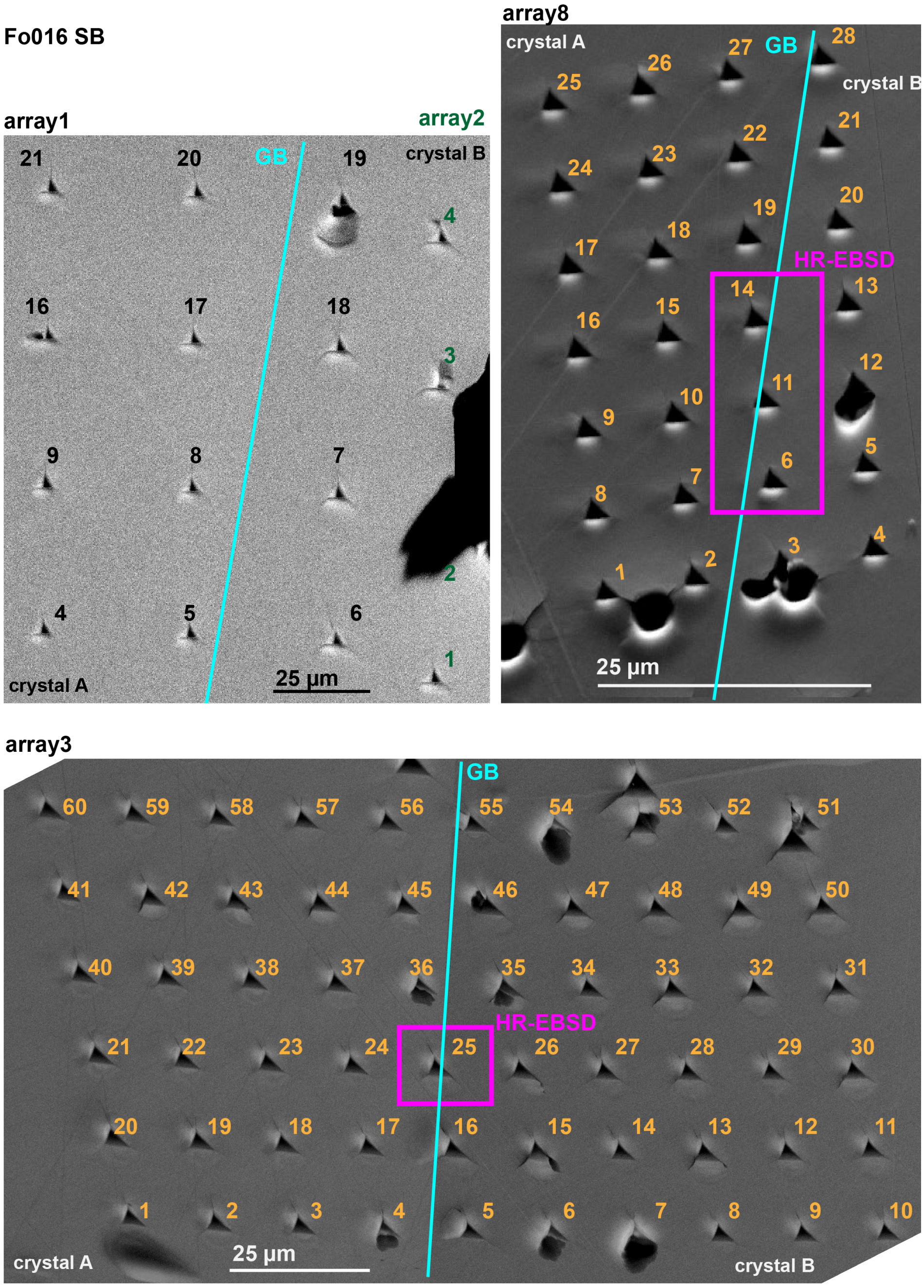

Figure A2. Backscatter images depicting the arrays placed in the SB sample with a sharp indenter as detailed in Table 1. The position of the further microstructural investigations with respect to the other indents and the grain boundary is marked by the magenta square. The numbers hear each indent correspond to the order in which the indents were placed.

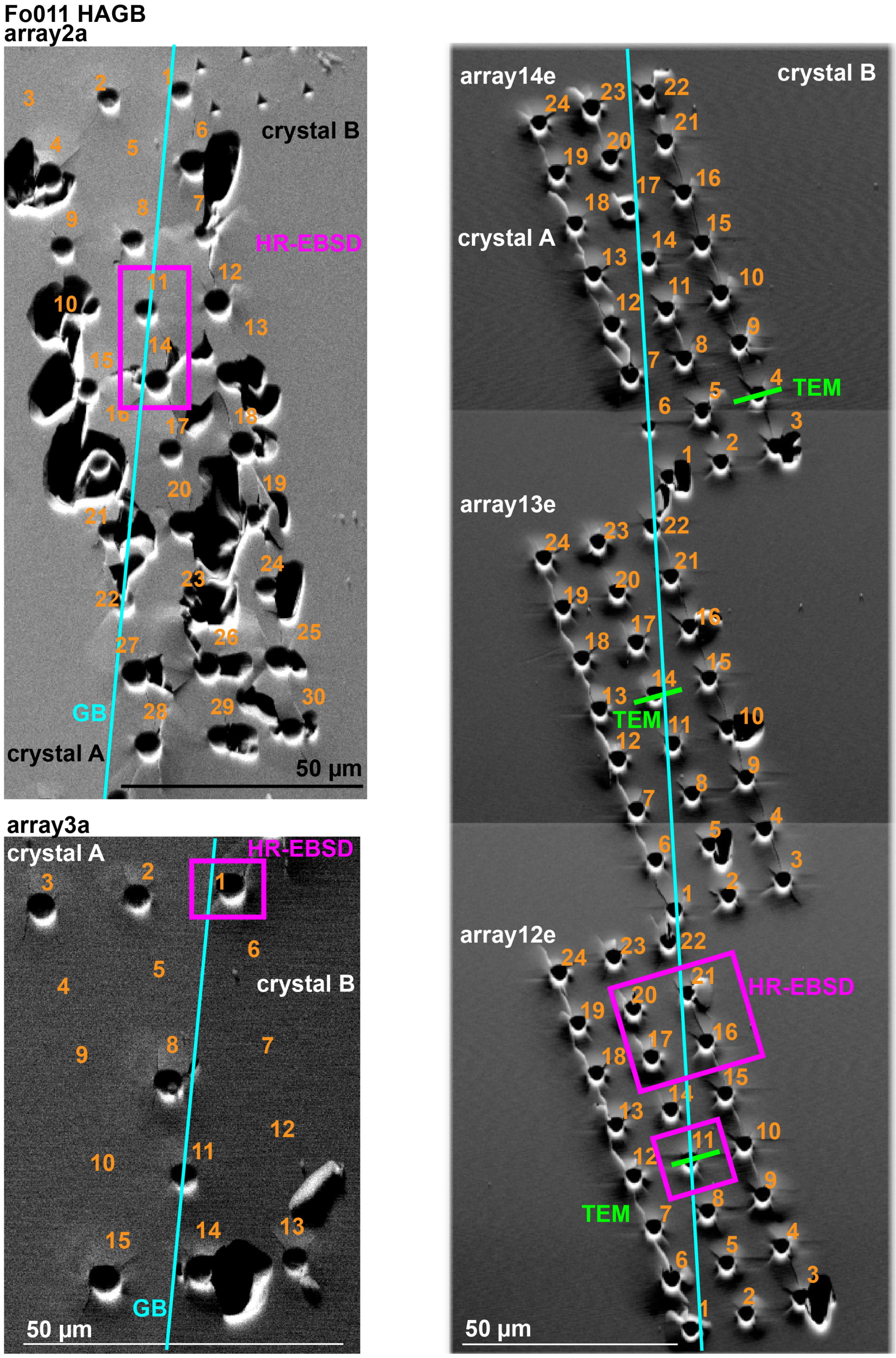

Figure A3. Backscatter images depicting the arrays placed in the HAGB sample with a spherical indenter as detailed in Table 1. The position of the further microstructural investigations with respect to the other indents and the grain boundary is marked by the magenta square. The numbers hear each indent correspond to the order in which the indents were placed.

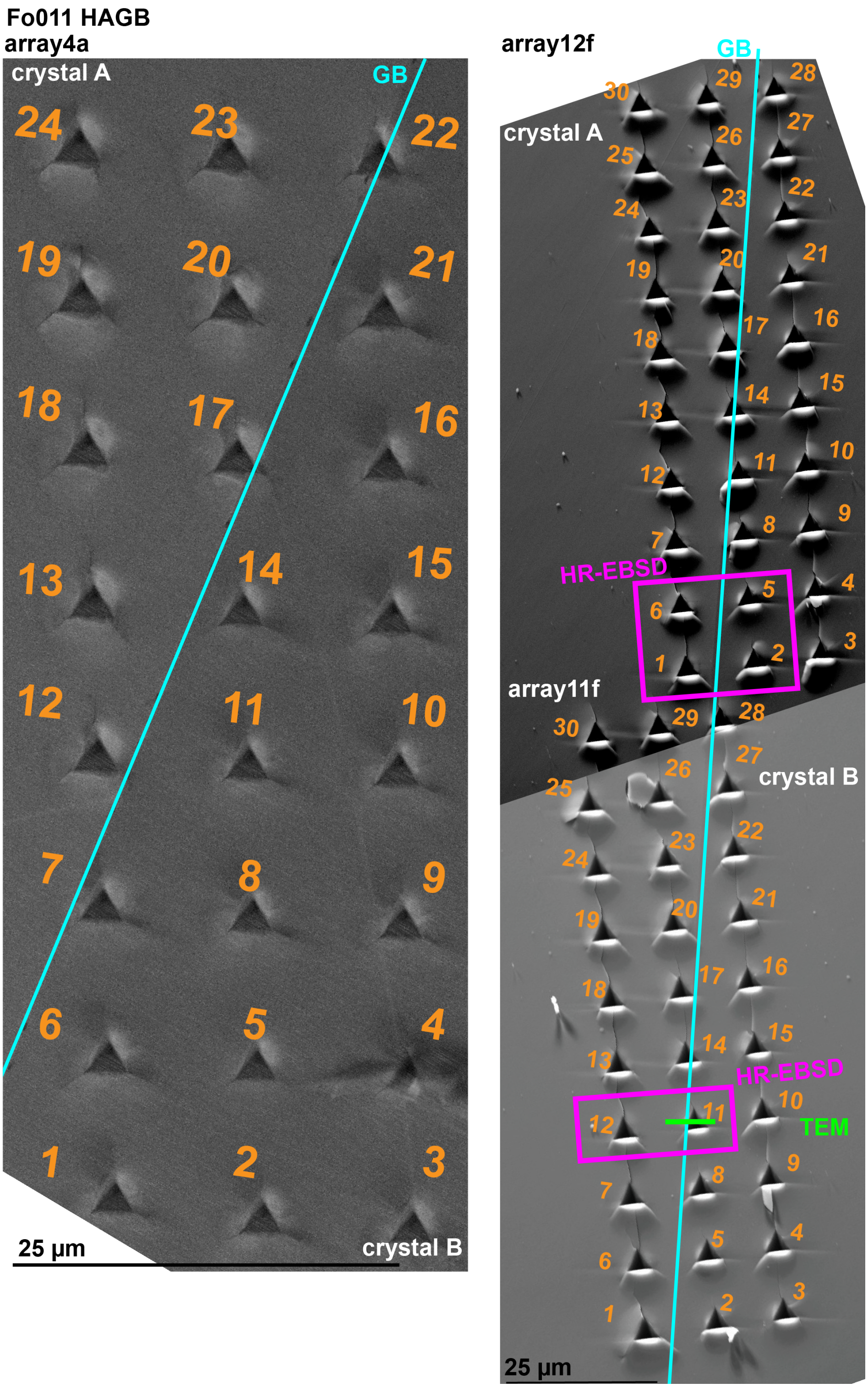

Figure A4. Backscatter images depicting the arrays placed in the HAGB sample with a sharp indenter. The position of the further microstructural investigations with respect to the other indents and the grain boundary is marked by the magenta square. The numbers hear each indent correspond to the order in which the indents were placed.

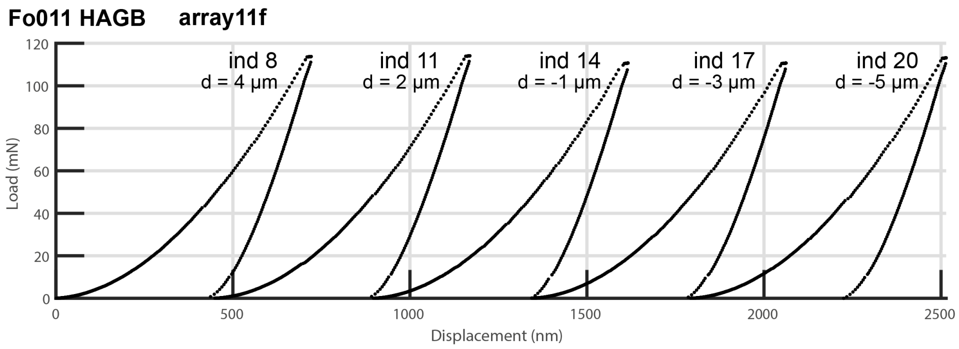

Figure A5. Examples of load-displacement curves collected with a Berkovich tip, arranged according to distance, d, from the grain boundary. The indents are part of array11f in Figure A4. Microstructural TEM investigations corresponding to indent 11 are presented in Figure 12 and HR-EBSD investigations are presented in Figure 7.

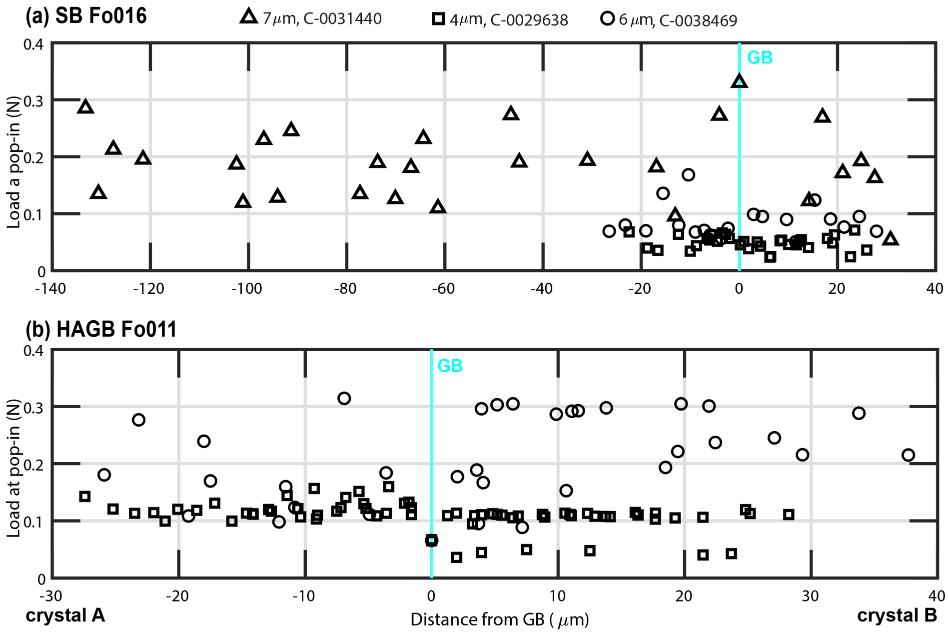

Figure A6. Load at pop-in in spherical indents placed in a) the SB sample and b) the HAGB sample displayed with respect to distance from the grain boundary. The indents without a pop-in are not displayed.

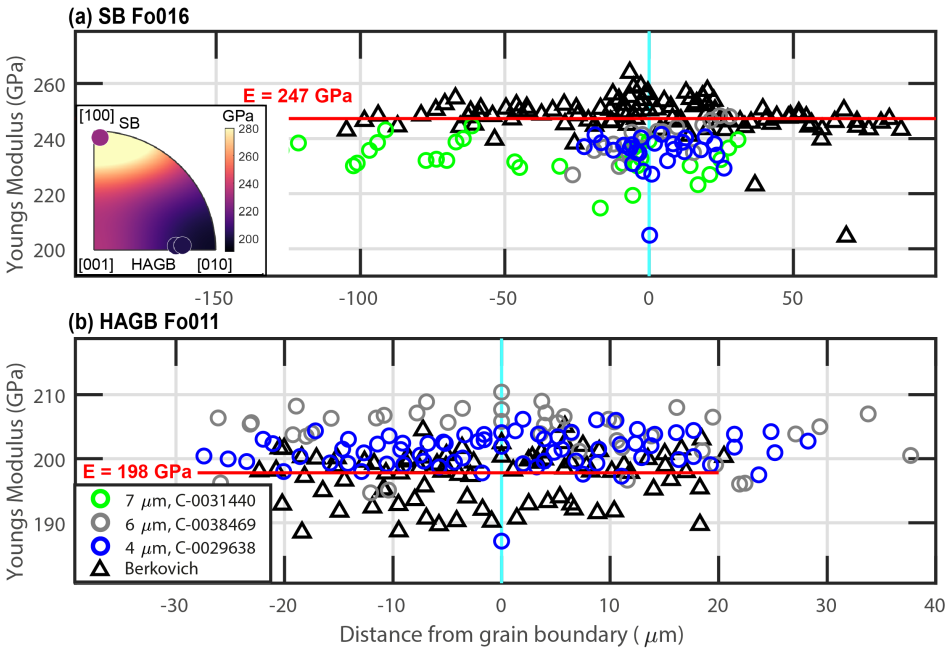

Figure A7. Results of Young's modulus calculations using Berkovich (open triangles) and spherical (open circles) nanoindentation in the a) subgrain boundary sample and b) high-angle boundary sample. The red line corresponds to the average value across all the data points. The Young's modulus is calculated fitting Equation 6 over the elastic loading segment for spherical nanoindentation data and using Equation 8 to average the value of Young's modulus over indentation depths greater than 200 nm for the Berkovich data. The insert in a) represents an inverse pole figure displaying the average values in both samples against a background coloured according to the theoretical Young's modulus from Abramson et al. (1997) for San Carlos olivine.

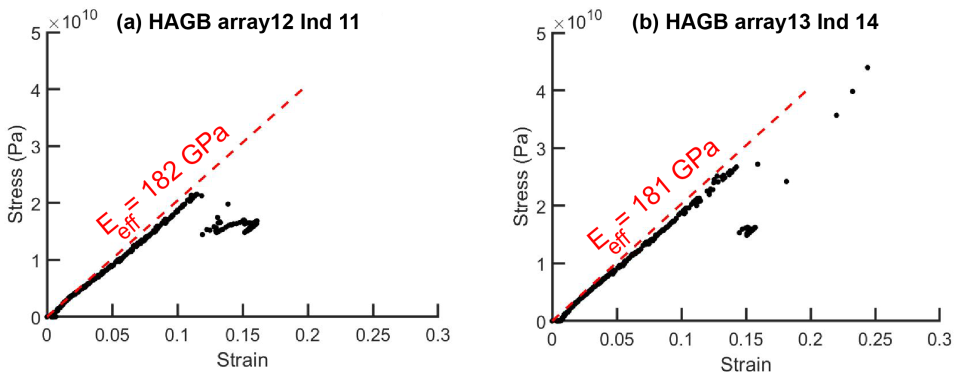

Figure A8. Stress-strain curves corresponding to the indents displayed in a) Figure 9 and Figure b) 10.

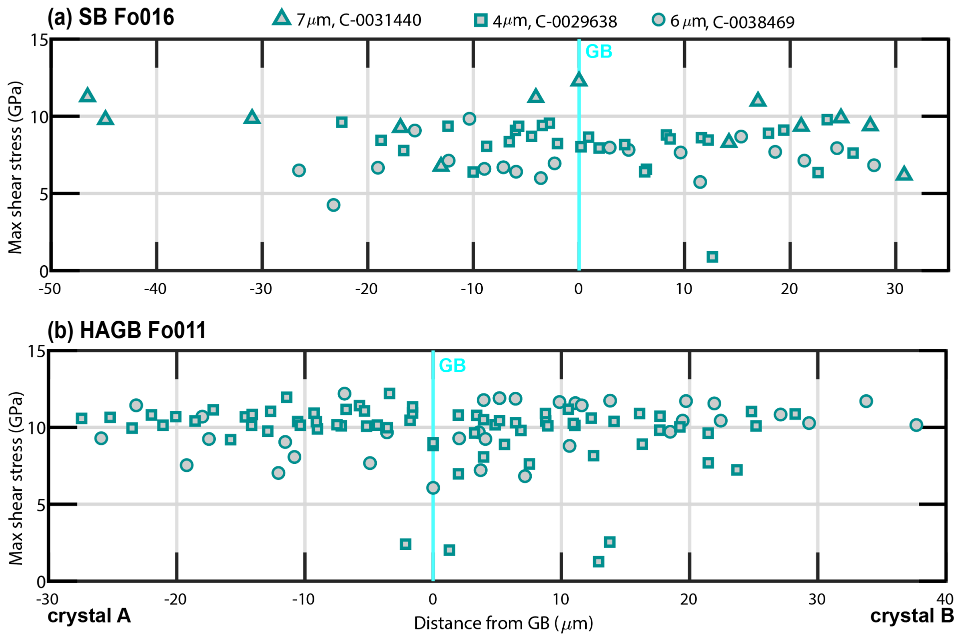

Figure A9. Shear stress calculated using the load at pop-in displayed in Figure A6 and Equation 7. For a general isotropic case, we can approximate the theoretical shear strength of a crystal with a Poisson's ratio of 0.24 as $E/15.57$ (e.g., Fang et al., 2021). Using the mean Young's modulus values in Figure A7 we can calculate the theoretical shear strength for the a) SB sample as 15.86 GPa and for the b) HAGB sample as 12.71 GPa. Note that in the single crystal, the shear stress for dislocation nucleation is closer to the theoretical limit compared to the shear stress corresponding to indents placed on the grain boundary.

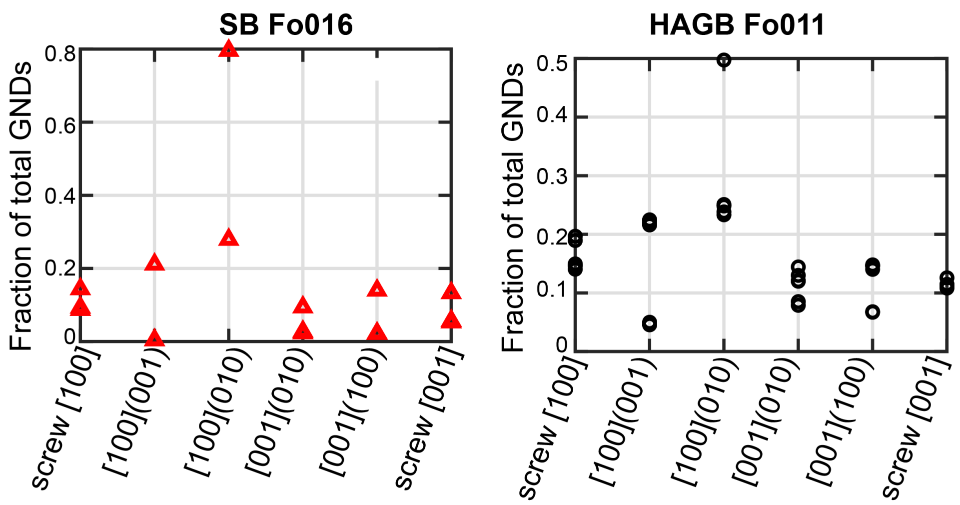

Figure A10. Fraction of total GNDs corresponding to each slip system accounted into the HR-EBSD calculation for olivine (Wallis et al., 2016) across the whole map area.

Authors' contributions

We report authors' contributions according to CRediT taxonomy.

Diana Avadanii: Writing - original draft preparation (lead); Formal analysis (lead); Writing – review and editing (equal); Investigation (lead); Visualisation (lead); Conceptualization (equal); Methodology (equal);

Lars Hansen: Supervision (lead); Conceptualization (lead); Resources (equal); Writing – review and editing (equal); Methodology (equal); Funding acquisition (lead);

Katharina Marquardt: Writing – review and editing (equal); Conceptualization (equal); Methodology (equal); Research samples (bicrystal synthesis); Funding acquisition (equal); Resources (equal); Investigation (supporting);

David Wallis: Writing – review and editing (equal); Investigation (supporting); Methodology (equal);

Markus Ohl: Writing – review and editing (supporting); Investigation (equal);

Angus Wilkinson: Supervision (equal); Conceptualization (equal); Resources (equal); Writing – review and editing (equal); Methodology (equal); Funding acquisition (equal);

Availability statement

The nanoindentation data presented in Section 3.1, and the HR-EBSD and TEM data presented in Section 3.2 in this study are available at the figshare.com repository via DOI 10.6084/m9.figshare.21507060 with the CC BY 4.0 licence.

References

Abramson, E., Brown, J., Slutsky, L., & Zaug, J. (1997). The elastic constants of san carlos olivine to 17 gpa. *Journal of Geophysical Research: Solid Earth*, *102*(B6), 12253–12263.

Adjaoud, O., Marquardt, K., & Jahn, S. (2012). Atomic structures and energies of grain boundaries in mg2sio4 forsterite from atomistic modeling. *Physics and Chemistry of Minerals*, *39*(9), 749–760.

Aifantis, K., Soer, W., De Hosson, J. T. M., & Willis, J. (2006). Interfaces within strain gradient plasticity: theory and experiments. *Acta Materialia*, *54*(19), 5077–5085.

Andani, M. T., Lakshmanan, A., Karamooz-Ravari, M., Sundararaghavan, V., Allison, J., & Misra, A. (2020). A quantitative study of stress fields ahead of a slip band blocked by a grain boundary in unalloyed magnesium. *Scientific reports*, *10*(1), 1–8.

A.P.Sutton, & R.W.Balluffi. (1995). *Interfaces in crystalline materials.* Oxford University Press.

Avadanii, D., Kareer, A., Hansen, L. N., & Wilkinson, A. J. (2022). Calibration and data analysis routines for nanoindentation with spherical. *in-prep*.

Bata, V., & Pereloma, E. V. (2004). An alternative physical explanation of the hall–petch relation. *Acta materialia*, *52*(3), 657–665.

Bayerschen, E., McBride, A., Reddy, B., & Böhlke, T. (2016). Review on slip transmission criteria in experiments and crystal plasticity models. *Journal of materials science*, *51*(5), 2243–2258.

Billen, M. I., & Hirth, G. (2007). Rheologic controls on slab dynamics. *Geochemistry, Geophysics, Geosystems*, *8*(8).

Bollinger, C., Marquardt, K., & Ferreira, F. (2019). Intragranular plasticity vs. grain boundary sliding (gbs) in forsterite: Microstructural evidence at high pressures (3.5–5.0 gpa). *American Mineralogist: Journal of Earth and Planetary Materials*, *104*(2), 220–231.

Breithaupt, T., Hansen, L., Wallis, D., & Armstrong, D. (2017). *Low-temperature plasticity of plagioclase from indentation* (Unpublished master's thesis). University of Oxford.

Britton, T., Randman, D., & Wilkinson, A. (2009). Nanoindentation study of slip transfer phenomenon at grain boundaries. *Journal of Materials Research*, *24*(3), 607–615.

Britton, T., & Wilkinson, A. (2011). Measurement of residual elastic strain and lattice rotations with high resolution electron backscatter diffraction. *Ultramicroscopy*, *111*(8), 1395–1404.

Britton, T., & Wilkinson, A. J. (2012). High resolution electron backscatter diffraction measurements of elastic strain variations in the presence of larger lattice rotations. *Ultramicroscopy*, *114*, 82–95.

Chen, S., Miyahara, Y., & Nomoto, A. (2018). Crystallographic orientation dependence of nanoindentation hardness in austenitic phase of stainless steel. *Philosoph-*

ical Magazine Letters, *98*(11), 473–485.

Cordero, Z. C., Knight, B. E., & Schuh, C. A. (2016). Six decades of the hall–petch effect–a survey of grain-size strengthening studies on pure metals. *International Materials Reviews*, *61*(8), 495–512.

Cottrell, A. H., & Bilby, B. A. (1949). Dislocation theory of yielding and strain ageing of iron. *Proceedings of the Physical Society. Section A*, *62*(1), 49.

Dehm, G., Jaya, B. N., Raghavan, R., & Kirchlechner, C. (2018). Overview on micro-and nanomechanical testing: New insights in interface plasticity and fracture at small length scales. *Acta Materialia*, *142*, 248–282.

Demouchy, S., Tommasi, A., Ballaran, T. B., & Cordier, P. (2013). Low strength of earth's uppermost mantle inferred from tri-axial deformation experiments on dry olivine crystals. *Physics of the Earth and Planetary Interiors*, *220*, 37–49.

Druiventak, A., Trepmann, C. A., Renner, J., & Hanke, K. (2011). Low-temperature plasticity of olivine during high stress deformation of peridotite at lithospheric conditions—an experimental study. *Earth and Planetary Science Letters*, *311*(3-4), 199–211.

England, P., & Molnar, P. (2015). Rheology of the lithosphere beneath the central and western tien shan. *Journal of Geophysical Research: Solid Earth*, *120*(5), 3803–3823.

Fang, X., Bishara, H., Ding, K., Tsybenko, H., Porz, L., Höfling, M., ... Durst, K. (2021). Nanoindentation pop-in in oxides at room temperature: dislocation activation or crack formation? *Journal of the American ceramic society*, *104*(9), 4728–4741.

Ferreira, F., Hansen, L. N., & Marquardt, K. (2021). The effect of grain boundaries on plastic deformation of olivine. *Journal of Geophysical Research: Solid Earth*, *126*(7), e2020JB020273.

Fischer-Cripps, A. C., & Nicholson, D. (2004). Nanoindentation. mechanical engineering series. *Appl. Mech. Rev.*, *57*(2), B12–B12.

Frost, H. J., & Ashby, M. F. (1982). *Deformation mechanism maps: the plasticity and creep of metals and ceramics*. Pergamon press.

Gaboriaud, R., Darot, M., Gueguen, Y., & Woirgard, J. (1981). Dislocations in olivine indented at low temperatures. *Physics and Chemistry of Minerals*, *7*(2), 100–104.

Gardés, E., Gibouin, D., Radiguet, B., David, A., Prellier, W., & Marquardt, K. (2021). Magnesium transport in olivine mantle: new insights from miniaturized study of volume and grain boundary diffusion in mg2sio4 bi-crystals. *Contributions to Mineralogy and Petrology*, *176*(12), 1–16.

Gardner, R., Piazolo, S., Evans, L., & Daczko, N. (2017). Patterns of strain localization in heterogeneous, polycrystalline rocks–a numerical perspective. *Earth and Planetary Science Letters*, *463*, 253–265.

Gleiter, H. (1977). The nature of dislocations in high-angle grain boundaries. *Philosophical Magazine*, *36*(5), 1109–1120.

Goetze, C., & Evans, B. (1979). Stress and temperature in the bending lithosphere as constrained by experimental rock mechanics. *Geophysical Journal International*, *59*(3), 463–478.

Guo, Y., Britton, T., & Wilkinson, A. (2014). Slip band–grain boundary interactions in commercial-purity titanium. *Acta Materialia*, *76*, 1–12.

Guo, Y., Collins, D. M., Tarleton, E., Hofmann, F., Wilkinson, A. J., & Britton, T. B. (2020). Dislocation density distribution at slip band-grain boundary intersections. *Acta Materialia*, *182*, 172–183.

Hall, E. (1951). The deformation and ageing of mild steel: Iii discussion of results. *Proceedings of the Physical Society. Section B*, *64*(9), 747.

Han, J., Thomas, S. L., & Srolovitz, D. J. (2018). Grain-boundary kinetics: A unified approach. *Progress in Materials Science*, *98*, 386–476.

Hansen, L., & Kohlstedt, D. L. (2015). 2.18 constitutive equations, rheological behavior, and viscosity of rocks. *Treatise on Geophysics, second edition*, *2*, 441–472.

Hansen, L., Kumamoto, K. M., Thom, C. A., Wallis, D., Durham, W. B., Goldsby, D. L., ... Kohlstedt, D. L. (2019). Low-temperature plasticity in olivine: Grain size, strain hardening, and the strength of the lithosphere. *Journal of Geophysical Research: Solid Earth*, *124*(6), 5427–5449.

Hartmann, K., Wirth, R., & Heinrich, W. (2010). Synthetic near $\sigma 5$ (210)/[100] grain boundary in yag fabricated by direct bonding: structure and stability. *Physics and Chemistry of Minerals*, *37*(5), 291–300.

Heinemann, S., Wirth, R., & Dresen, G. (2001). Synthesis of feldspar bicrystals by direct bonding. *Physics and Chemistry of Minerals*, *28*(10), 685–692.

Heinemann, S., Wirth, R., Gottschalk, M., & Dresen, G. (2005). Synthetic [100] tilt grain boundaries in forsterite: 9.9 to 21.5. *Physics and chemistry of minerals*, *32*(4), 229–240.

Hirth, J. P. (1972). *The influence of grain boundaries on mechanical properties.* Springer.

Hook, R., & Hirth, J. (1967). The deformation behavior of isoaxial bicrystals of fe-3% si. *Acta Metallurgica*, *15*(3), 535–551.

Hunter, J., & Watts, A. (2016). Gravity anomalies, flexure and mantle rheology seaward of circum-pacific trenches. *Geophysical Journal International*, *207*(1), 288–316.

Idrissi, H., Bollinger, C., Boioli, F., Schryvers, D., & Cordier, P. (2016). Low-temperature plasticity of olivine revisited with in situ tem nanomechanical testing. *Science advances*, *2*(3), e1501671.

Javaid, F., Pouriayevali, H., & Durst, K. (2021). Dislocation–grain boundary interactions: Recent advances on the underlying mechanisms studied via nanoindentation testing. *Journal of Materials Research*, *36*(12), 2545–2557.

Johnson, K. (1970). The correlation of indentation experiments. *Journal of the Mechanics and Physics of Solids*, *18*(2), 115–126.

Kacher, J., Eftink, B., Cui, B., & Robertson, I. (2014). Dislocation interactions with grain boundaries. *Current Opinion in Solid State and Materials Science*, *18*(4), 227–243.

Kalidindi, S. R., & Pathak, S. (2008). Determination of the effective zero-point and the extraction of spherical nanoindentation stress–strain curves. *Acta Materialia*, *56*(14), 3523–3532.

Kalidindi, S. R., & Vachhani, S. J. (2014). Mechanical characterization of grain boundaries using nanoindentation. *Current Opinion in Solid State and Materials Science*, *18*(4), 196–204.

Katayama, I., & Karato, S.-i. (2008). Low-temperature, high-stress deformation of olivine under water-saturated conditions. *Physics of the Earth and Planetary Interiors*, *168*(3-4), 125–133.

Koizumi, S., Hiraga, T., & Suzuki, T. S. (2020). Vickers indentation tests on olivine: size effects. *Physics and Chemistry of Minerals*, *47*(2), 1–14.

Korenaga, J. (2020). Plate tectonics and surface environment: Role of the oceanic upper mantle. *Earth-Science Reviews*, *205*, 103185.

Kumamoto, K. M., Thom, C. A., Wallis, D., Hansen, L. N., Armstrong, D. E., Warren, J. M., ... Wilkinson, A. J. (2017). Size effects resolve discrepancies in 40 years of work on low-temperature plasticity in olivine. *Science advances*, *3*(9), e1701338.

Lee, T., Robertson, I., & Birnbaum, H. (1989). Prediction of slip transfer mechanisms across grain boundaries. *Scripta metallurgica*, *23*(5), 799–803.

Lee, T., Robertson, I., & Birnbaum, H. (1990). Anin situ transmission electron microscope deformation study of the slip transfer mechanisms in metals. *Metallurgical Transactions A*, *21*(9), 2437–2447.

Li, J. (1963). Petch relation and grain boundary sources. *Transactions of the Metallurgical Society of AIME*, *227*(1), 239.

Li, J., Pharr, G. M., & Kirchlechner, C. (2021). Quantitative insights into the dislocation source behavior of twin boundaries suggest a new dislocation source mechanism. *Journal of Materials Research*, *36*(10), 2037–2046.

Li, T., Gao, Y., Bei, H., & George, E. P. (2011). Indentation schmid factor and orientation dependence of nanoindentation pop-in behavior of nial single crystals. *Journal of the Mechanics and Physics of Solids*, *59*(6), 1147–1162.

Li, W., Bei, H., Qu, J., & Gao, Y. (2013). Effects of machine stiffness on the loading–displacement curve during spherical nano-indentation. *Journal of Materials Research*, *28*(14), 1903–1911.

Li, Y., Bushby, A. J., & Dunstan, D. J. (2016). The hall–petch effect as a manifestation of the general size effect. *Proceedings of the Royal Society A: Mathematical, Physical and Engineering Sciences*, *472*(2190), 20150890.

Liu, Y., King, H. E., Van Huis, M. A., Drury, M. R., & Plümper, O. (2016). Nanotomography of porous geological materials using focused ion beam-scanning electron microscopy. *Minerals*, *6*(4), 104.

Luster, J., & Morris, M. (1995). Compatibility of deformation in two-phase ti-al alloys: Dependence on microstructure and orientation relationships. *Metallurgical and Materials Transactions A*, *26*(7), 1745–1756.

Maaß, R., & Derlet, P. (2018). Micro-plasticity and recent insights from intermittent and small-scale plasticity. *Acta Materialia*, *143*, 338–363.

Marquardt, K., & Faul, U. H. (2018). The structure and composition of olivine grain boundaries: 40 years of studies, status and current developments. *Physics and Chemistry of Minerals*, *45*(2), 139–172.

Marquardt, K., Rohrer, G. S., Morales, L., Rybacki, E., Marquardt, H., & Lin, B. (2015). The most frequent interfaces in olivine aggregates: the gbcd and its importance for grain boundary related processes. *Contributions to Mineralogy and Petrology*, *170*(4), 1–17.

Mei, S., Suzuki, A., Kohlstedt, D., Dixon, N., & Durham, W. (2010). Experimental constraints on the strength of the lithospheric mantle. *Journal of Geophysical Research: Solid Earth*, *115*(B8).

Meyersm, M. A., & Ashworth, E. (1982). A model for the effect of grain size on the yield stress of metals. *Philosophical Magazine A*, *46*(5), 737–759.

Mitchell, T. (1979). Application of transmission electron microscopy to the study of deformation in ceramic oxides. *Journal of the American Ceramic Society*, *62*(5-6), 254–267.

Morris, J. R., Bei, H., Pharr, G. M., & George, E. P. (2011). Size effects and stochastic behavior of nanoindentation pop in. *Physical review letters*, *106*(16), 165502.

Murr, L. (1975). Some observations of grain boundary ledges and ledges as dislocation sources in metals and alloys. *Metallurgical Transactions A*, *6*(3), 505–513.

Murr, L. (1981). Strain-induced dislocation emission from grain boundaries in stainless steel. *Materials Science and Engineering*, *51*(1), 71–79.

Mussi, A., Cordier, P., & Demouchy, S. (2015). Characterization of dislocation interactions in olivine using electron tomography. *Philosophical Magazine*, *95*(4), 335–345.

Mussi, A., Cordier, P., Demouchy, S., & Vanmansart, C. (2014). Characterization of the glide planes of the [001] screw dislocations in olivine using electron tomography. *Physics and Chemistry of Minerals*, *41*(7), 537–545.

Mussi, A., Nafi, M., Demouchy, S., & Cordier, P. (2015). On the deformation mechanism of olivine single crystals at lithospheric temperatures: an electron tomography study. *European Journal of Mineralogy*, *27*(6), 707–715.

Ohl, M., Plümper, O., Chatzaras, V., Wallis, D., Vollmer, C., & Drury, M. (2020). Mechanisms of fault mirror formation and fault healing in carbonate rocks. *Earth and Planetary Science Letters*, *530*, 115886.

Ohmura, T., & Tsuzaki, K. (2007). Plasticity initiation and subsequent deformation behavior in the vicinity of single grain boundary investigated through nanoindentation technique. *Journal of materials science*, *42*(5), 1728–1732.

Oliver, W. C., & Pharr, G. M. (1992). An improved technique for determining hardness and elastic modulus using load and displacement sensing indentation experiments. *Journal of materials research*, *7*(6), 1564–1583.

Pathak, S., & Kalidindi, S. R. (2015). Spherical nanoindentation stress–strain curves. *Materials science and engineering: R: Reports*, *91*, 1–36.

Petch, N. (1953). The cleavage strength of polycrystals. *Journal of the iron and steel institute*, *174*, 25–28.

Phakey, P., Dollinger, G., & Christie, J. (1972). Transmission electron microscopy of experimentally deformed olivine crystals. *Washington DC American Geophysical Union Geophysical Monograph Series*, *16*, 117–138.

Piazolo, S., Bons, P. D., Griera, A., Llorens, M.-G., Gomez-Rivas, E., Koehn, D., ... others (2019). A review of numerical modelling of the dynamics of microstructural development in rocks and ice: Past, present and future. *Journal of Structural Geology*, *125*, 111–123.

Pleus, A., Ito, G., Wessel, P., & Frazer, L. N. (2020). Rheology and thermal structure of the lithosphere beneath the hawaiian ridge inferred from gravity data and models of plate flexure. *Geophysical Journal International*, *222*(1), 207–224.

Price, C., & Hirth, J. (1972). A mechanism for the generation of screw dislocations from grain-boundary ledges. *Materials science and engineering*, *9*, 15–18.

Raterron, P., Wu, Y., Weidner, D. J., & Chen, J. (2004). Low-temperature olivine rheology at high pressure. *Physics of the Earth and Planetary Interiors*, *145*(1-4), 149–159.

Sangal, S., Kurzydlowski, K., & Tangri, K. (1991). The effect of extrinsic grain boundary dislocations on the grain size strengthening in polycrystals. *Acta metallurgica et materialia*, *39*(6), 1281–1288.

Sangid, M. D., Ezaz, T., Sehitoglu, H., & Robertson, I. M. (2011). Energy of slip transmission and nucleation at grain boundaries. *Acta materialia*, *59*(1), 283–296.

Schmid, E., & Boas, W. (1950). Plasticity of crystals.

Shen, Z., Wagoner, R., & Clark, W. (1986). Dislocation pile-up and grain boundary interactions in 304 stainless steel. *Scripta metallurgica*, *20*(6), 921–926.

Thieme, M., Demouchy, S., Mainprice, D., Barou, F., & Cordier, P. (2018). Stress evolution and associated microstructure during transient creep of olivine at 1000–1200 c. *Physics of the Earth and Planetary Interiors*, *278*, 34–46.

Tommasi, A., Mainprice, D., Canova, G., & Chastel, Y. (2000). Viscoplastic self-consistent and equilibrium-based modeling of olivine lattice preferred orientations: Implications for the upper mantle seismic anisotropy. *Journal of Geophysical Research: Solid Earth*, *105*(B4), 7893–7908.

Vachhani, S. J., Doherty, R. D., & Kalidindi, S. R. (2016). Studies of grain boundary regions in deformed polycrystalline aluminum using spherical nanoindentation. *International Journal of Plasticity*, *81*, 87–101.

Varin, R., Kurzydlowski, K., & Tangri, K. (1987). Analytical treatment of grain boundary sources for dislocations. *Materials Science and Engineering*, *85*, 115–126.

Voyiadjis, G. Z., & Zhang, C. (2015). The mechanical behavior during nanoindentation near the grain boundary in a bicrystal fcc metal. *Materials Science and Engineering: A*, *621*, 218–228.

Wallis, D., Hansen, L. N., Britton, T. B., & Wilkinson, A. J. (2016). Geometrically necessary dislocation densities in olivine obtained using high-angular resolution electron backscatter diffraction. *Ultramicroscopy*, *168*, 34–45.

Wallis, D., Hansen, L. N., Britton, T. B., & Wilkinson, A. J. (2019). High-angular resolution electron backscatter diffraction as a new tool for mapping lattice distortion in geological minerals. *Journal of Geophysical Research: Solid Earth*, *124*(7), 6337–6358.

Wallis, D., Hansen, L. N., Kumamoto, K. M., Thom, C. A., Plümper, O., Ohl, M., ... others (2020). Dislocation interactions during low-temperature plasticity of olivine and their impact on the evolution of lithospheric strength. *Earth and Planetary Science Letters*, *543*, 116349.

Wang, M., & Ngan, A. (2004). Indentation strain burst phenomenon induced by grain boundaries in niobium. *Journal of materials research*, *19*(8), 2478–2486.

Watts, A., & Zhong, S. (2000). Observations of flexure and the rheology of oceanic lithosphere. *Geophysical Journal International*, *142*(3), 855–875.

Wilkinson, A. J. (2006). High resolution measurements of strain and tilt distributions in sige mesas using electron backscatter diffraction. *Applied physics letters*, *89*(24), 241910.

Wilkinson, A. J., Meaden, G., & Dingley, D. J. (2006). High-resolution elastic strain measurement from electron backscatter diffraction patterns: new levels of sensitivity. *Ultramicroscopy*, *106*(4-5), 307–313.